

1                   **Modeling impacts of dust mineralogy on fast climate response**

Deleted: Earth's Radiation and Climate

2

3 Qianqian Song<sup>1</sup>, Paul Ginoux<sup>2</sup>, Maria Gonçalves Ageitos<sup>3,4</sup>, Ron L. Miller<sup>5,6</sup>, Vincenzo Obiso<sup>5</sup>,  
4 Carlos Pérez García-Pando<sup>4,7</sup>

5 <sup>1</sup> Atmospheric and Oceanic Sciences Program, Princeton University, Princeton, NJ, USA

6 <sup>2</sup> NOAA Geophysical Fluid Dynamics Laboratory, Princeton, NJ, USA

7 <sup>3</sup> Projects and Construction Engineering Department. Universitat Politècnica de Catalunya-Barcelona  
8 TECH, Terrassa, Spain

9 <sup>4</sup> Barcelona Supercomputing Center, Barcelona, Spain

10 <sup>5</sup> NASA Goddard Institute for Space Studies, New York, NY, USA

11 <sup>6</sup> Department of Applied Physics and Applied Mathematics, Columbia University, New York, NY, USA

12 <sup>7</sup> ICREA, Catalan Institution for Research and Advanced Studies, Barcelona, Spain

13 Correspondence: Qianqian Song (qs7080@princeton.edu)

## 15 Abstract

16 Mineralogical composition drives dust impacts on Earth's climate systems. However, most climate  
17 models still use homogeneous dust, without accounting for the temporal and spatial variation in  
18 mineralogy. To quantify the radiative impact of resolving dust mineralogy on Earth's climate, we  
19 implement and simulate the distribution of dust minerals (i.e., illite, kaolinite, smectite, hematite,  
20 calcite, feldspar, quartz, and gypsum) from Claquin et al. (1999) (C1999) and activate their  
21 interaction with radiation in the GFDL AM4.0 model. Resolving mineralogy reduces dust  
22 absorption compared to the homogeneous dust used in the standard GFDL AM4.0 model that  
23 assumes a globally uniform hematite volume content of 2.7% (HD27). The reduction in dust  
24 absorption results in improved agreement with observation-based single scattering albedo (SSA),  
25 radiative fluxes from CERES (the Clouds and the Earth's Radiant Energy System), and land  
26 surface temperature from CRU (Climatic Research Unit), compared to the baseline HD27 model  
27 version. It also results in distinct radiative impacts on Earth's climate over North Africa. Over the  
28 19-year (from 2001 to 2019) modeled period during JJA (June-July-August), the reduction in dust  
29 absorption in AM4.0 leads to a reduction of over 50% in net downward radiation across the Sahara  
30 and approximately 20% over the Sahel at top of atmosphere (TOA) compared to the baseline HD27  
31 model version. The reduced dust absorption weakens the atmospheric warming effect of dust  
32 aerosols and leads to an alteration in land surface temperature, resulting in a decrease of 0.66 K  
33 over the Sahara and an increase of 0.7 K over the Sahel. The less warming in the atmosphere  
34 suppresses ascent and weakens the monsoon inflow from the Gulf of Guinea. This brings less  
35 moisture to the Sahel, which combined with decreased ascent induces a reduction of precipitation.  
36 To isolate the effect of reduced absorption, compared to resolving spatial and temporal mineralogy,  
37 we carry out a simulation where the hematite volume content of homogeneous dust is reduced  
38 from 2.7% to 0.9% (HD09). The dust absorption (e.g., single scattering albedo) of HD09 is  
39 comparable to that of the mineralogically speciated model on a global mean scale, albeit with a  
40 lower spatial variation that arises solely from particle size. Comparison of the two models indicates  
41 that the spatial inhomogeneity in dust absorption resulting from resolving mineralogy does not  
42 have significant impacts on Earth's radiation and climate, provided there is a similar level of dust  
43 absorption on a global mean scale before and after resolving dust mineralogy. However,  
44 uncertainties related to emission and distribution of minerals may blur the advantages of resolving  
45 minerals to study their impact on radiation, cloud properties, ocean biogeochemistry, air quality,

Deleted: diverse

Deleted: fixed

Deleted: mineralogy

Deleted: its

Deleted: dust

Deleted: and

Deleted: bulk dust

Deleted: it

Deleted: ).

Deleted: 4K

Deleted: 6K

Deleted: Interestingly, we find similar results by simply fixing the hematite content of dust to 0.9% by volume, which is more computationally efficient than simulating all minerals....

61 and photochemistry. On the other hand, lumping together clay minerals (i.e., illite, kaolinite, and  
62 smectite), but excluding externally mixed hematite and gypsum, appears to provide both  
63 computational efficiency and relative accuracy. Nevertheless, for specific research, it may be  
64 necessary to fully resolve mineralogy to achieve accuracy.

## 65 1 Introduction

66 Soil dust aerosols emitted from erodible land surfaces, hereafter referred to as dust, are the most  
67 abundant aerosol component in the atmosphere in terms of dry mass. Dust has significant impacts on  
68 the Earth's climate systems (atmosphere, ocean, cryosphere) due to its interaction with terrestrial and  
69 solar radiation (Sokolik and Toon, 1999), cloud microphysics (Guo et al., 2021), tropospheric  
70 chemistry (Bian and Zender, 2003; Paulot et al., 2016), and oceanic and terrestrial  
71 biogeochemistry (Mahowald, 2011; Evans et al., 2019; Dunne et al., 2020). In addition, dust particles  
72 deposited on snow and ice decrease surface reflectivity and accelerate snowmelt (Skiles et al., 2018;  
73 Réveillet et al., 2022). Dust can influence Earth's radiative energy budget through different pathways;  
74 among them: 1) directly by interacting with both solar and terrestrial radiation (i.e., direct radiative  
75 effects, hereafter referred to as DRE) 2) by radiatively influencing the thermal dynamical structure of  
76 atmosphere and thereby clouds (i.e., semi-direct radiative effect) and 3) indirectly by altering cloud  
77 reflectivity (cloud albedo effect) and lifetime (cloud lifetime effect). Unfortunately, the quantitative  
78 estimate of dust DRE at the top of atmosphere (TOA) is largely uncertain (Claquin et al., 1998; Miller  
79 et al., 2014; Kok et al., 2017; Song et al., 2022). A significant part of this uncertainty has been attributed  
80 to neglecting variations in dust mineralogical composition and its evolution during transport (Li et al.,  
81 2021).

82 The magnitude of dust impacts on the Earth's climate systems depends on its mineralogical  
83 composition, as has been shown in multiple studies. In the ShortWave (SW), dust absorption depends  
84 on the iron oxides content. Sokolik and Toon (1999) suggested that a small amount of iron oxides  
85 internally mixed with less absorptive minerals is able to reverse the sign of  $DRE_{SW}$  at TOA from  
86 negative (cooling effect) to positive (warming effect). Multiple studies have confirmed the importance  
87 of iron oxides to the dust  $DRE_{SW}$  (Balkanski et al., 2007; Li et al., 2021; Obiso et al., 2023). In  
88 LongWave (LW) spectrum, absorption and  $DRE_{LW}$  depend on the abundance of quartz, calcite, and  
89 clays in coarse and super-coarse modes (Di Biagio et al., 2017; Sokolik and Toon, 1999). As a result,  
90 resolving dust mineralogy allows to better understand the impact of dust DRE, such as the fast response  
91 of the land surface temperature, as opposed to the slow response of sea surface temperature that will

**Deleted:** As a result, resolving dust mineralogy allows to better understand the impact of dust DRE, such as the fast response (i.e., the response with fixed sea surface temperature) of the Earth's surface radiation (Persad et al., 2014), land surface temperature, precipitation (Ming et al., 2010), and atmospheric circulation. Dust absorption can also affect the slow climate response (i.e., the response including changes in sea surface temperature) of the Earth surface temperature (Miller and Tegen, 1998), precipitation, ocean heat transport (Ocko et al., 2014), which may affect hurricane genesis (Strong et al., 2018), and induce feedback (Miller et al., 2004; Miller et al., 2014).

104 not be studied here. This fast temperature response will affect precipitation, and atmospheric  
105 circulation (Ming et al., 2010; Persad et al., 2014).

106 In addition, resolving dust mineralogy is also crucial for studying heterogeneous reactions of acid gases  
107 with dust aerosols. For example, the uptake of  $\text{HNO}_3$ ,  $\text{NO}_3^-$ ,  $\text{N}_2\text{O}_5$  on dust particles is suggested to be  
108 limited by alkalinity that comprises calcium and magnesium carbonates (Song and Carmichael, 2001;  
109 Paulot et al., 2016). These reactions will modify the composition of dust particles and subsequently  
110 changing their hygroscopicity, cloud condensation nucleation (CCN), and ice nucleation activities  
111 (Kelly et al., 2007), and thereby further affecting precipitation (Rosenfeld et al., 2001). Moreover,  
112 heterogeneous reactions with mineral dust could significantly affect tropospheric photochemical  
113 oxidation cycles, causing up to 10% reduction in  $\text{O}_3$  concentrations in dust source regions and nearby  
114 (Dentener et al., 1996). Among the different minerals, K-Feldspar appears to dominate ice nucleation,  
115 despite being a minor component of aeolian dust (Atkinson et al., 2013; Harrison et al., 2019), although  
116 other minerals such as quartz may also contribute (Chatziparaschos et al., 2023). The key factor  
117 controlling the production and removal of pollutants and the damages by acid rain is the pH of  
118 raindrops, which has been observed to increase due to its dependency on Ca-rich dust (Grider et al.,  
119 2023).

120 Despite the potential importance of resolving dust mineralogy in various aspects, current climate  
121 models tend to use a fixed mineralogy without considering the temporal and spatial variations in  
122 dust mineralogical composition. To test the importance of resolving dust mineralogy on the fast  
123 climate response (e.g., surface temperature response over land, atmospheric circulation and  
124 precipitation response) through its interactions with SW and LW radiation (i.e., through dust DRE),  
125 dust mineralogy has been implemented and simulated in the GFDL AM4.0 model (Zhao et al.,  
126 2018a, b), including its on-line interactions with radiation. Following the pioneering work of  
127 Claquin et al. (1999) (C1999), we consider the emission, transport and interactions with radiation  
128 and deposition of eight minerals: illite, kaolinite, smectite, hematite, calcite, feldspar, quartz and  
129 gypsum. Following the recent launch of the Earth Surface Mineral Dust Source Investigation  
130 (EMIT) instrument specifically designed to retrieve global distribution of dust mineralogy over  
131 dust sources (Green et al., 2020), there have been coordinated efforts to represent dust mineralogy  
132 and investigate DRE of mineral-speciated dust in climate models, in particular in Li et al. (2021),  
133 Gonçalves Ageitos et al. (2023), and Obiso et al. (2023). However, to the best of our knowledge,  
134 there have been no studies investigating the fast climate impact of dust while accounting for its

135 mineral speciation. Our work contributes to these efforts by incorporating dust mineralogy into the  
136 GFDL models, and it is distinguished by extending its investigation to the fast climate response of  
137 mineral-speciated dust. The impacts of dust mineralogy on other aspects, such as sea surface  
138 temperature and slow climate response, heterogeneous reactions, and ice nucleation ability, will  
139 be examined in future studies.

Deleted: joins

Deleted: , with the additional focus on studying

Deleted: resolving

Deleted: mineralogy to dust DRE

140 Section 2 provides the description of the GFDL AM4.0 model and dust mineralogy  
141 implementation. Section 3 describes our experimental design. In Section 4, we calculate mineral  
142 optical properties, activate the interaction of minerals with radiation in GFDL AM4.0 and compare  
143 modeled dust optical properties with observations. Section 5 presents the impacts of resolving dust  
144 mineralogy on Earth's radiation and climate with a focus on the North Africa, as well as their  
145 evaluations. In Section 6, we investigate the influences of reducing the number of mineral tracers.  
146 Section 7 provides a summary of the study along with the main conclusions.

Deleted: 6

## 147 2 Model and Data

### 148 2.1 Model description

149 We conduct a series of experiments with GFDL AM4.0 (Zhao et al., 2018a, b) over the period  
150 2001-2019. These experiments use the AMIP protocol, where sea surface temperature (SST) and  
151 sea-ice are imposed based upon average monthly observations (see Gates, 1992 for details).

Deleted: Atmospheric Model Intercomparison Project (AMIP; Gates, 1992)

152 Observed gridded SST and sea-ice concentration boundary conditions are from the reconstructions  
153 of Taylor et al., (2000). Historical reconstructions of monthly solar spectral irradiances are from  
154 Matthes et al., (2017). For radiation calculations, global monthly mean concentrations of  
155 greenhouse gases (GHGs), including nitrous oxide (N<sub>2</sub>O), and ozone-depleting substances (ODSs,  
156 including CFC-11, CFC-12, CFC-113, and HCFC-22) are specified from Meinshausen et al.,  
157 (2017). The solar irradiances and GHG databases are standard for CMIP6. Longwave (LW)  
158 scattering of aerosols is not accounted for in the model.

159 In AM4.0, dust emission is calculated interactively following the parameterization of Ginoux et al.  
160 (2001) with a threshold of wind erosion and global scaling factor of  $3.5 \text{ m s}^{-1}$  and  $0.2 \mu\text{g s}^2 \text{ m}^{-5}$ ,  
161 respectively. Dust size is represented by five bins with diameter ranging from  $0.2 \mu\text{m}$  to  $20 \mu\text{m}$   
162 (bin1:  $0.2 - 2 \mu\text{m}$ , bin2:  $2 - 3.6 \mu\text{m}$ , bin3:  $3.6 - 6 \mu\text{m}$ , bin4:  $6 - 12 \mu\text{m}$ , bin5:  $12 - 20 \mu\text{m}$ ). The

170 corresponding source fractions have been updated from 0.1, 0.225, 0.225, 0.225 and 0.225 to  
171 values of 0.04, 0.14, 0.19, 0.49, and 0.14 for the **five bins. These updated source functions allocate**  
172 more fraction to coarser size bins, following the suggested Brittle Fragmentation Theory (BFT) as  
173 proposed by Kok et al. (2011). Dust mineral composition in the standard AM4.0 is considered as  
174 uniform, with no temporal and spatial variations; in other words, dust Refractive Index (RI) is  
175 temporally and spatially homogeneous (case referred to as homogeneous dust hereafter). The dust  
176 RI in the standard AM4.0 is taken from Balkanski et al., (2007), assuming a fixed hematite content  
177 of 2.7% by volume (HD27), which was calculated for the internal mixture of hematite and five  
178 other minerals (calcite, quartz, illite, kaolinite and montmorillonite) using the Maxwell Garnett  
179 mixing rule (see details in Balkanski et al., 2007). The decision to fix the hematite content for dust  
180 particles at 2.7% was made during the development of the previous GFDL Climate Model CM3  
181 (Donner et al., 2011). This decision was prompted by the discovery that dust absorption was  
182 unrealistically high (by a factor 3) in CM2 (Delworth et al., 2006) compared to AERONET  
183 observations (Balkanski et al., 2007). In CM3, the conjunction of a sharp decrease of black carbon  
184 (strong aerosol absorber) with a new emission inventory and the switch to more scattering dust  
185 had a negative effect on precipitation bias, and late 20th century warming (see Donner et al., 2011  
186 for details). To mitigate this bias, the selection of 2.7% hematite was adopted in CM3, as well as  
187 in the subsequent GFDL models. The control run conducted with the homogeneous dust in the  
188 standard AM4.0 model is labeled as HD27 as described in Table 2.

189 In addition, we conduct simulations assuming homogeneous dust with hematite content of 0.9%  
190 by volume, with RI from Balkanski et al. (2007). Similar to HD27, this experiment, labeled as  
191 HD09 in Table 2, does not account for the temporal and spatial variations in dust mineralogy.

## 192 2.2 Dust mineralogy implementation

193 Claquin et al. (1999) (C1999) is the earliest study providing a soil mineralogy map oriented toward  
194 atmospheric and climate modelling. The soil map provides the mineral mass fractions present in  
195 the clay and silt size ranges for eight different minerals, namely: illite, smectite, kaolinite, calcite,  
196 quartz, feldspars, gypsum, and hematite. In this study, we implement the eight minerals from the  
197 soil mineralogy map provided by C1999 in GFDL AM4.0 to resolve dust mineralogy. The soil  
198 map is based on soil analyses that are usually done after wet sieving, which disperse mineral  
199 aggregates into small particles. This dispersal is particularly relevant for the phyllosilicates,

**Deleted:** corresponding source fractions.

**Deleted:** is

**Deleted:** a Maxwell-Garnett mixing rule. The control run conducted with the standard AM4.0 model is labeled as HD27 as described in Table 2.

**Deleted:** (C1999) is the earliest study providing a soil mineralogy map oriented toward atmospheric and climate modelling. The soil map provides the mineral mass fractions present in the clay and silt size ranges for eight different minerals, namely: illite, smectite, kaolinite, calcite, quartz, feldspars, gypsum, and hematite. In this study, we implement the eight minerals from the soil map provided by C1999, in GFDL AM4.0 to resolve dust (for more details see Ginoux et al. 2023, in preparation). The soil map is based on soil analyses that are usually done after wet sieving, which disperse mineral aggregates into small particles. We apply an algorithm based on Brittle Fragmentation Theory (BFT; Kok, 2011) to reconstruct the mineral aggregates emitted from the original undispersed soils. The mass density of the eight minerals, along with a brief description of their importance to Earth's climate, are listed in Table 1. The density of minerals impacts their settling velocity, which is relevant to the removal of particles in the atmosphere. Iron oxides, represented by hematite in C1999, have larger density than other minerals, so that hematite deposits more quickly and is not able to be transported to remote regions when not aggregated or internally mixed with lighter clay minerals. Moreover, hematite is the strongest absorber in the visible. As such, the correct representation of hematite content in dust aerosols is critical in improving the representation of dust interaction with SW radiation in climate models. Considering that iron oxides are usually found as accretions in other minerals, particularly phyllosilicates (clay minerals): illite, kaolinite and smectite (Zhang et al., 2015; Panta et al., 2023), we partition hematite into two portions: internally mixed hematite and externally mixed hematite, in terms of their mixing state with clay minerals. For accretions, we take the 5% mass fraction of hematite in the mixture at emission as a reference to estimate the amount of internally mixed hematite (following Gonçalves Ageitos et al., 2023). Specifically, hematite is internally mixed with clay minerals for the portion of its mass fraction at emission that is less than 5%, while it is considered externally mixed for the portion that exceeds 5%.<sup>¶</sup>

244 typically found in the form of aggregates in soils. They are detected in the atmosphere with higher  
245 proportions at coarser (silt) sizes than those reported in the soil maps (Perlwitz et al., 2015b; Perez  
246 Garcia-Pando et al., 2016). These recent studies also show that the Brittle Fragmentation Theory  
247 (BFT; Kok, 2011) represents a practical framework to generate the emitted particle size  
248 distribution based on the dispersed soil PSD, which facilitates the utilization of soil mineralogy  
249 maps. In our simulations, we employ BFT to reconstruct the mineral aggregates emitted from the  
250 original undispersed soils, following the methods described in Gonçalves Ageitos et al., 2023. The  
251 mass density of the eight minerals, along with a brief description of their importance to Earth's  
252 climate, are listed in Table 1. The density of minerals impacts their settling velocity, which is  
253 relevant to the removal of particles in the atmosphere. Goethite and hematite are the two major  
254 types of iron oxides present in soils. Goethite is less absorptive than hematite and is not resolved  
255 in C1999. So, iron oxides are represented by hematite in this study. Hematite has larger density  
256 than other minerals, so that hematite deposits more quickly and is not able to be transported to  
257 remote regions when not aggregated or internally mixed with lighter clay minerals. Moreover,  
258 among the minerals considered here, hematite is the strongest absorber at ultraviolet (UV) and  
259 visible wavelengths, while it does not have noticeable absorption at infrared wavelengths (IR)  
260 compared to other minerals (Sokolik and Toon, 1999). As such, the correct representation of  
261 hematite content in dust aerosols is critical in improving the representation of dust interaction with  
262 SW radiation in climate models. All minerals are considered to be externally mixed, except for  
263 iron oxides. A large part of the emitted flux of iron oxides is considered to be internally mixed  
264 with other minerals, e.g., in the form of accretions in phyllosilicates, in line with observational  
265 evidence and previous modeling studies (Kandler et al., 2009; Perlwitz et al., 2015a; Zhang et al.,  
266 2015; Panta et al., 2023). As suggested by Gonçalves Ageitos et al. (2023), we define two different  
267 types of tracers for the iron oxides: one set of tracers carries the mass of the hematite that  
268 constitutes small accretions in clay minerals (i.e., internally mixed with clay minerals), are allowed  
269 to be up to 5 % of the masses of their host minerals at emission (Perlwitz et al., 2015a; Gonçalves  
270 Ageitos et al., 2023). Given the low fractional mass of hematite compared to their host minerals,  
271 we assume that these accretions do not change the density of their host particles. These internally  
272 mixed accretions form the largest fraction of the emitted hematite. Another smaller set of tracers  
273 carries the mass of the remaining fraction of hematite, which is considered to be externally mixed  
274 with the other minerals, including the internal mixtures of hematite with clay.

275 In addition to the similar roles of clay minerals in carrying iron oxides, the optical properties of  
276 the three clay minerals are very similar, and ~~the~~ optical properties of ~~their~~ external mixture ~~are~~  
277 found to be almost identical to their internal mixture (see Section S1 in the Supplement). This  
278 finding ~~suggests the use of~~ a single mineral species to represent all three clay minerals in their  
279 interaction with radiation to reduce computational cost. Therefore, the optical properties of one  
280 single mineral (clay433) are used to represent the optical properties of all three clay minerals. ~~The~~  
281 ~~clay433 represents a mixed mineral comprising three clay minerals: illite, kaolinite and smectite,~~  
282 ~~with mass fraction of 40%, 30%, and 30%, respectively (see detailed descriptions in~~  
283 ~~Supplementary Section S1). This simplification streamlines~~ the calculations of optical properties  
284 for internal mixtures of hematite and ~~the three clay minerals (illite, kaolinite, and smectite),~~  
285 reducing it from an internal mixture of four minerals (hematite, illite, kaolinite and smectite) to an  
286 internal mixture of two minerals (hematite and clay433).

287 ~~The optical properties of the internal mixture of hematite and clay433 are calculated using three~~  
288 ~~mixing rules: volume weighted average (VOL-mixing), Maxwell-Garnett mixing rule (MG-~~  
289 ~~mixing) and Bruggeman mixing rule (BM-mixing). Generally, VOL-mixing is used for a quasi-~~  
290 ~~homogeneous mixture, that is when the components have similar refractive index. For cases~~  
291 ~~involving dominant homogeneous host with small inclusions of contrasting composition, MG-~~  
292 ~~mixing is appropriate. BM-mixing is suitable for mixtures that the inclusions virtually occupy the~~  
293 ~~entire volume of the particle, and the host disappears. The detailed discussion regarding the three~~  
294 ~~mixing rules and their applications can be found in Liu and Daum (2008) and Markel (2016). The~~  
295 ~~appropriate selection of mixing rules is important for the determination of the optical properties of~~  
296 ~~the mixtures. Therefore, we incorporate all three mixing rules in this study. These calculations are~~  
297 ~~performed for various volume mixing fractions of hematite with respect to clay433, to construct a~~  
298 ~~lookup table (LUT) for each mixing rule. The optical properties of each mineral as well as the~~  
299 ~~internal mixtures of hematite and clay433 are calculated offline using Mie code with a spherical~~  
300 ~~shape assumption. As all other minerals have similar SW absorption, internal or external mixing~~  
301 ~~does not change their absorption properties. So, we assume all other minerals to be externally~~  
302 ~~mixed. More details about optical properties of minerals will be discussed in Section 4.~~

303 Overall, we implement nine types of mineral tracers: seven non-hematite minerals along with  
304 distinguished internal and external hematite, as listed in Table 1. Each type is distributed across

Deleted: their

Deleted: the

Deleted: is

Deleted: implies that we could

Deleted: , see descriptions in Supplementary Section S1

Deleted: This simplifies

Deleted: ,

Deleted: The optical properties of the internal mixture of hematite and clay433 are calculated using three mixing rules: volume weighted average (VOL-mixing), Maxwell-Garnett mixing rule (MG-mixing) and Bruggeman mixing rule (BM-mixing). These calculations are performed for various volume mixing fractions of hematite with respect to clay433, to construct a lookup table for each mixing rule. The optical properties of each mineral as well as the internal mixtures of hematite and clay433 are calculated offline using Mie code with a spherical shape assumption. As all other minerals have similar SW absorption, internal or external mixing does not change their absorption properties. So, we assume all other minerals to be externally mixed.



325 five size bins. As a result, 45 mineral tracers have been incorporated in AM4.0 to account for dust  
 326 mineralogy.

327 Table 1. The list of minerals considered in this study and their importance to Earth’s climate. Mineral-  
 328 dependent mass densities are defined following Table 1 in Gonçalves Ageitos et al. (2023), in which the  
 329 references of mineral densities are listed.

Minerals	Density (kg/m <sup>3</sup> )	Importance
1. Hematite (int.)	2570	It is the strongest visible absorber. It is internally mixed with clay minerals when its mass fraction at emission < 5%.
2. Hematite (ext.)	4770 <sup>(1)</sup>	It is externally mixed for the part of emitted mass fraction > 5%.
Three clay minerals: 3. Illite 4. Smectite 5. Kaolinite  Clay in BM-RT	2570 2570 2630  2590	They are the most abundant mineral components in clay-sized (diameter < 2μm) minerals. They are internally mixed with internal hematite.  The three clay minerals are lumped together as one mineral species ‘clay’ in the BM-RT experiment in Section 6.
6. Calcite	2710	It is important for chemistry. (e.g., heterogeneous reaction with acidic gases and formation of sulfate and nitrates on the surface of dust particles, and cloud droplet pH)
7. Feldspar	2680	A fraction of feldspar (K-feldspar) is important for ice nucleation
8. Quartz	2670	It is the most abundant mineral component in silt-sized (diameter:2-63 μm) minerals. It is important for LW absorption and ice nucleation.
9. Gypsum	2308	It possibly has impact on chemistry, but the impact is likely unimportant given the low abundance globally.

<sup>(1)</sup>We use the mean of hematite and goethite densities for hematite, as in Gonçalves Ageitos et al. (2023).

Field Code Changed

330 **2.3 AERONET Dust SSA**

331 The AERONET Version 3 Level 2.0 Almuqantar **inversion** retrievals (Giles et al., 2019; Sinyuk et  
 332 al., 2020) from 2000 to 2020 are screened for dust events following the methodology in Gonçalves  
 333 Ageitos et al. (2023) and Obiso et al. (2023). This screening process aims to select dust-dominated  
 334 events and filter out the AERONET scenes contaminated by other absorbing aerosols. The criteria  
 335 that are applied to AERONET retrievals to screen dust events are: 1) hourly retrievals from  
 336 AERONET are considered to represent dust when the fine volume fraction is small (below 15%),  
 337 2) the SSA increases from 440 nm to 675 nm (a feature that distinguishes dust from other species,  
 338 see Dubovik et al., 2002), and 3) the mean of the imaginary index at red and near-infrared

339 wavelengths (675, 870 and 1020 nm) is lower than 0.0042 (as higher values would indicate the  
340 presence of absorbing black and brown carbon, following Schuster et al., 2016). We calculate  
341 AERONET SSA in the visible by averaging AERONET retrieved SSA at two visible wavelengths  
342 (0.44  $\mu\text{m}$  and 0.67  $\mu\text{m}$ ) weighted by solar spectrum, following Eq. (2).

Deleted: .

## 343 2.4 Laboratory Dust SSA

344 The lab measured dust SSA at 550 nm is obtained from Di Biagio et al. (2019) (DB-2019 hereafter),  
345 in which dust SSA was directly retrieved from scattering and absorption measurements. We  
346 acknowledge the limits of laboratory measurements, where the dust samples are not aerosols  
347 present in the atmosphere, but instead are reemitted in the lab from soil samples collected from  
348 various source regions. Consequently, the laboratory measurements in DB-2019 do not account  
349 for dust aerosols transported from other regions to the regions of interest. In addition, in contrast  
350 to the modeled dust diameter range of 0.2  $\mu\text{m}$  to 20 $\mu\text{m}$ , DB-2019 measures dust particles with a  
351 diameter ranging from 0.2  $\mu\text{m}$  up to 10 $\mu\text{m}$ .

## 352 2.5 CERES Data

353 To compare modeled fluxes at TOA with observations, we use the Clouds and the Earth's Radiant  
354 Energy System (CERES) Energy Balanced and Filled (EBAF) Edition-4.2 data (Loeb et al., 2018).  
355 The standard CERES level-3 products provide clear-sky fluxes by averaging all CERES footprints  
356 within a region that are completely free of clouds. Therefore, there are many missing regions in  
357 monthly mean clear-sky TOA flux maps because completely cloud-free conditions are not always  
358 observed at the CERES footprint scale ( $\sim 20$  km at nadir). In contrast to the standard CERES level-  
359 3 products, CERES\_EBAF product infers clear-sky fluxes from clear portions of partly cloudy  
360 CERES footprints thereby producing a clear-sky TOA flux climatology free of any missing regions  
361 (details in Loeb et al., 2018). Starting from CERES\_EBAF\_Ed4.1, the product also provides clear-  
362 sky flux estimates for the total region (i.e., the total CERES footprints) by combining CERES  
363 observations and radiative transfer calculations, which represents clear-sky flux with clouds  
364 removed from the entire atmospheric column of CERES footprints. These clear-sky fluxes for the  
365 total region are defined in a way that is more consistent with how clear-sky fluxes are represented  
366 in climate models (for details see CERES\_EBAF\_Ed4.1 Data Quality Summary). In this study,  
367 the monthly mean TOA 'Clear-Sky Flux Estimate for Total Region' variables in the  
368 CERES\_EBAF\_Ed4.2 product, the most recent version of the product, are used to compare with

370 modeled monthly mean clear-sky flux at TOA. The comparisons allow us to examine the  
 371 agreement of modeled clear-sky fluxes from different experiments with observations. The  
 372 comparison results will be shown in section 5.1.

### 373 2.6 CRU TS Data

374 The CRU TS (Climatic Research Unit gridded Time Series) dataset provides high-resolution (0.5°  
 375 latitude × 0.5° longitude) climate dataset over land except Antarctica. The dataset is based on  
 376 extensive networks of weather stations going back to 1901(Harris et al., 2020). This dataset has  
 377 been widely used in various research areas since its first release in 2000. The mean 2-meter  
 378 temperature (TMP) and precipitation rate (PRE) variables from CRU TS v4.07 are used to evaluate  
 379 our model simulations. The results will be shown in section 5.2 and section 5.3.

## 380 3 Experimental Design

381 Table 2. List of experiments and their description. Experiments are named based on the type of dust used  
 382 or the mixing rules for minerals applied in each experiment.

Experiments	Dust or Minerals	Description	Optics
HD27	HD27	Dust refractive index is spatially and temporally uniform. Dust is assumed to contain 2.7% of hematite by volume. Its optical properties are used to represent dust in the standard GFDL AM4.0 model.	Balkanski et al. (2007)
HD09	HD09	Dust refractive index is spatially and temporally uniform. Dust is assumed to contain 0.9% of hematite by volume.	Balkanski et al. (2007)
VOL	VOL-mixing	Soil mineralogy from C1999 is implemented in AM4.0. Hematite (int.) is internally mixed with clay minerals following the volume-weighted mean mixing rule.	Scanza et al. (2015)
MG	MG-mixing	Soil mineralogy from C1999 is implemented in AM4.0. Hematite (int.) is internally mixed with clay minerals following the Maxwell Garnett mixing rule.	Scanza et al. (2015)
BM	BM-mixing	Soil mineralogy from C1999 is implemented in AM4.0. Hematite (int.) is internally mixed with clay minerals following the Bruggeman mixing rule.	Scanza et al. (2015)
BM-RT	BM-mixing	Three experiments are performed step by step to reduce the number of mineral tracers. 1) BM-LC experiment: following BM experiment, illite, kaolinite and smectite are lumped together as one tracer 'clay'.	Scanza et al. (2015)

		2) BM-LCRH experiment: following BM-LC, <u>the tracer of external mixed hematite is removed, its mass is combined with internal mixed hematite.</u>	
		3) BM-LCRHRG experiment: following BM-LCRH, gypsum <u>tracer is removed, and its mass is proportionally added to all other remaining minerals.</u>	

Deleted: further

Deleted: further

383 We conduct a total of six experiments using the GFDL AM4.0 model, with each experiment's  
 384 description provided in Table 2. Two of these experiments serve as control runs in which dust  
 385 aerosols are represented with temporally and spatially fixed composition in the model. The first  
 386 control run, referred to as HD27, represents how dust aerosols are implemented in the standard  
 387 GFDL AM4.0 model (Zhao et al., 2018a). The second control run is the HD09, in which dust is  
 388 more scattering than that in the standard AM4.0 model (i.e., HD27) due to its reduced hematite  
 389 volume fraction from 2.7% to 0.9%.

390 The other three experiments, namely VOL, MG, and BM, resolve dust mineralogy and activate  
 391 their interaction with radiation. These three experiments incorporate 45 mineral tracers for nine  
 392 types of mineral tracers distributed over five size bins, as described in Section 2.2. Additionally,  
 393 we conduct the BM-RT experiments, which consist of three sub-experiments: BM-LC, BM-LCRH,  
 394 BM-LCRHRG. These experiments aim to explore the potential of reducing mineral tracers, which  
 395 can improve the model computational efficiency. The results will be discussed in Section 6.

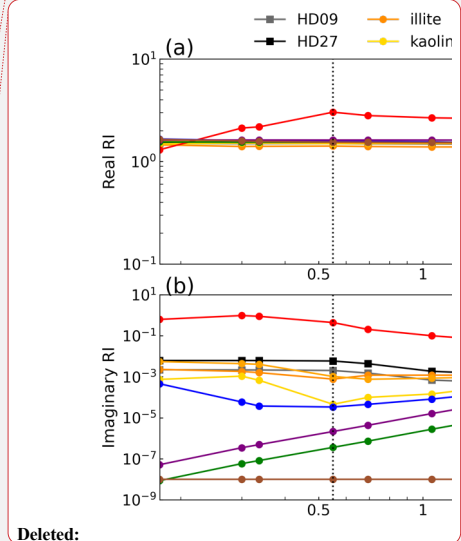
Deleted: .

Field Code Changed

Deleted: for each contrasting pair.

Deleted: from

396 Each of the experiments ran for 19 years, from 2001 to 2019. We consider the 19-year runs of the  
 397 experiment as a group of simulations, containing 19 members of one-year simulation. The two  
 398 control runs (i.e., HD27 and HD09), combined with the three mineral-resolved experiments (i.e.,  
 399 VOL, MG, and BM), form a total of six contrasting pairs. In this study, for each contrasting pair,  
 400 we define the anomaly as the group mean difference (based on 19-year mean) between mineral-  
 401 resolved experiment and control run. An anomaly is considered statistically significant if the p-  
 402 value, determined by the student's t-test between the two contrasting groups of simulations, is  
 403 smaller than 0.05.

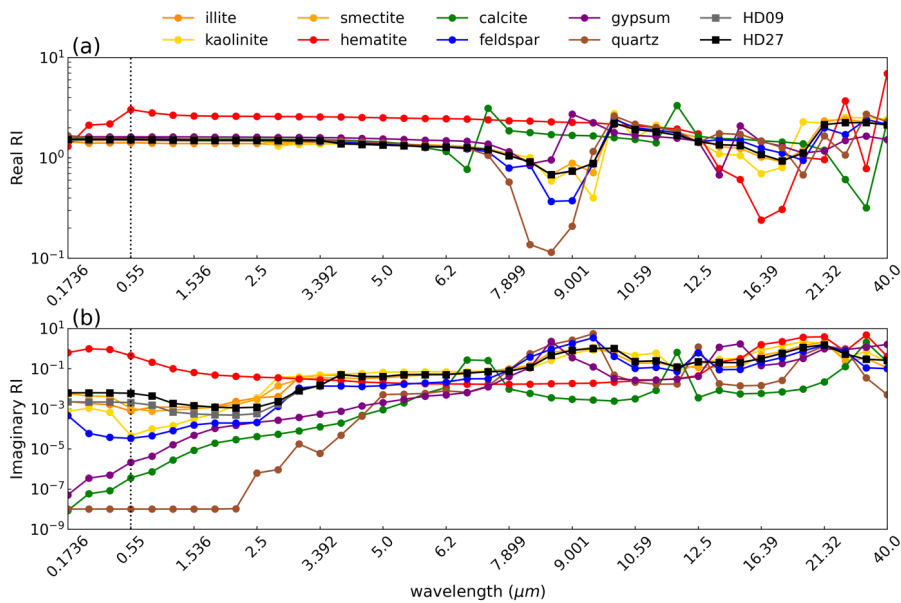


Deleted:

## 404 4 Optical Properties

### 405 4.1 Dust optical properties

406



413  
 414 Figure 1. Real part and imaginary part of complex refractive indices (RI) of two homogeneous dust (e.g.,  
 415 HD27 and HD09) and eight minerals (Scanza et al., 2015). The dotted lines represent the real part (a) and  
 416 imaginary part (b) of dust or minerals for the corresponding wavelength. The black and grey dotted lines  
 417 are for HD27 and HD09, respectively. The colorful dotted lines are for the eight minerals.  
 418 We use the refractive indices (RI) of each mineral from Scanza et al. (2015) and the RI of HD27  
 419 and HD09 from Balkanski et al. (2007) to calculate the LUT of optical properties. The spectral RI  
 420 of each mineral and homogeneous dust (e.g., HD27 and HD09) are shown in Figure 1. The HD09  
 421 dust has lower imaginary part of RI at 550 nm than HD27 dust, indicating its lower absorption in  
 422 the visible band due to a reduced content of hematite.  
 423 After calculating LUT of optical properties (details in Section 2.2), we incorporate the interaction  
 424 of minerals with radiation into GFDL AM4.0. The modeled emission, load, deposition, and  
 425 lifetime for each mineral are provided in Table S1 in the Supplement. Table 3 provides global  
 426 total dust emission, load, globally averaged dust aerosol optical depth (DAOD) and SSA for each  
 427 experiment listed in Table 2, and their comparisons with previous studies. DAOD and SSA from  
 428 AM4.0 simulations are averaged in the visible band (0.44 - 0.625μm) of GFDL AM4.0. Unless  
 429 otherwise specified, DAOD and SSA in this study refer to the average in the visible band. Note

**Deleted:** i.  
**Deleted:** Figure 1 shows the refractive indices (RI) of each mineral (Scanza et al., 2015) as well as the RI of two homogeneous dust mixtures HD27 and HD09 (Balkanski et al., 2007). The HD09 dust has lower imaginary part of RI at 550 nm than HD27 dust, indicating its lower absorption in the visible band due to a reduced content of hematite. With the optical properties of each mineral component calculated...  
**Deleted:** .  
**Deleted:** Table 3 provides the  
**Deleted:** . DAOD and SSA from AM4.0 simulations are averaged in the visible band (0.44-0.625μm) of GFDL AM4.0. Note that in our calculations, the domain averaged DAOD is always weighted by the area of each grid cell. The domain averaged SSA is always weighted by the area and DAOD of each grid cell. Additionally, the spectral-averaged DAOD and SSA are always weighted by solar spectrum, which peaks at around 0.50 μm. The emission, load, deposition, and lifetime for each mineral are provided in Table S1 in the Supplement. The subtle difference in DAOD and large variation in dust SSA across experiments suggests that resolving dust mineralogy or changing hematite content in homogeneous dust does not affect visible extinction of dust aerosols (i.e., DAOD). However, it significantly affects the relative strength of dust absorption versus scattering. The variation in total dust emission and DAOD across different experiments results from the feedback of dust interactions with radiation (Miller et al., 2004

459 that in our calculations, the domain averaged DAOD is always weighted by the area of each grid  
 460 cell. The domain averaged SSA is always weighted by the area and DAOD of each grid cell.  
 461 Additionally, the spectrally averaged DAOD and SSA are always weighted by the TOA solar  
 462 radiation intensity at the corresponding wavelengths, peaking around 0.50 μm, as shown in Eq. (1)  
 463 and Eq. (2).

$$DAOD = \frac{\int_{\lambda_1}^{\lambda_2} DAOD(\lambda) B(\lambda) d\lambda}{\int_{\lambda_1}^{\lambda_2} B(\lambda) d\lambda} \quad \text{Eq. (1)}$$

$$SSA = \frac{\int_{\lambda_1}^{\lambda_2} SSA(\lambda) DAOD(\lambda) B(\lambda) d\lambda}{\int_{\lambda_1}^{\lambda_2} B(\lambda) DAOD(\lambda) d\lambda} \quad \text{Eq. (2)}$$

464 Where  $B(\lambda)$  describes the solar radiation energy intensity, which can be calculated by means of  
 465 the Planck's function  $B(T,\lambda)$ , using the temperature of the Sun ( $T = 5800$  K).

466 Table 3. 19-year (2001-2019) averaged global dust emission, load, globally averaged visible band dust  
 467 optical depth (DAOD) and single scattering albedo (SSA) for each experiment in this study. We use each  
 468 grid-cell surface area as a weight for the global DAOD average. We use each grid-cell surface area times  
 469 DAOD in each grid-cell as a weight for the global SSA average. In addition, we include the results from  
 470 previous studies for the purpose of comparison. Note, the modeled DAOD and SSA in this study are  
 471 averaged in the visible band (0.44 - 0.625 μm) of GFDL AM4.0, while averaged in the UV-VIS band (0.30  
 472 - 0.77 μm) of GISS ModelE2.1 in Obiso et al. (2023).

Experiments		Emission (Tg/ yr)	Load (Tg)	DAOD	SSA
HD27		3354	23.6	0.022	0.86
HD09		3119	21.5	0.020	0.93
VOL		3154	21.6	0.022	0.91
MG		3083	21.1	0.021	0.93
BM		3087	21.1	0.021	0.93
BM-RT	BM-LC	3097	21.1	0.021	0.930
	BM-LCRH	3069	20.9	0.021	0.930
	BM-LCRHRG	3110	21.4	0.021	0.928
AeroCom <sup>(1)</sup>		1600 (1000-3200)	20 (9-26)	0.029 (0.021 - 0.035)	-
CMIP5 <sup>(2)</sup>		2700 (1700-3700)	17 (14-36)	=	=

Moved down [1]: ; Pérez et al., 2006; Miller et al., 2014), which is influenced by the distinct scattering properties of dust aerosols in each experiment

Moved down [2]: in VOL suggests that VOL-mixing dust is more absorptive than MG-mixing and BM-mixing dust. This finding is consistent with previous studies that have suggested that VOL-mixing method, when applied to minerals to compute the bulk aerosol optical properties, may artificially enhance absorption relative to scattering and lead to a lower SSA for bulk dust aerosol (Zhang et al., 2015).

Deleted: . The HD27 dust used in the standard AM4.0 model is the most absorptive among all experiments. The HD09 dust is much less absorptive due to its smaller hematite content, thereby resulting in a lower imaginary part of RI in the visible range (Figure 1). We can see that the SSA of HD09 dust is very similar to the values obtained in cases where minerals are resolved (i.e., MG and BM). For the three mineral-resolved experiments, the lower global mean SSA...

Deleted: DAOD)

Deleted: SSA)

Deleted: -

Deleted: -

Deleted: DAOD

Deleted: SSA

Deleted: 023

Deleted: 1123  
(500 - 4400)

Deleted: 15.8  
(7-30)

Deleted: 023

Deleted: 01

Deleted: 053

<u>CMIP6<sup>(3)</sup></u>		<u>3472</u>	<u>25</u>	<u>0.029</u>	<u>-</u>
<u>DUSTCOMM<sup>(4)</sup></u>		<u>4700</u> <u>(3300 - 9000)</u>	<u>26</u> <u>(22 - 31)</u>	<u>0.028</u> <u>(0.024 - 0.030)</u>	<u>-</u>
GISS ModelE2.1 <sup>(5)</sup>	HOM	4031	31.3	0.020	0.917
	EXT	4152	32.4	0.020	0.936
	INT	4284	33.7	0.021	0.942
<p><u>(1) Results are from AeroCom Phase I, which were taken from Table 3 in Huneceus et al. (2011), and the 1 standard error range was obtained by eliminating the two highest and lowest values.</u></p> <p><u>(2) Results are from Table 3 in Wu et al. (2020)</u></p> <p><u>(3) Results from Zhao et al. (2022)</u></p> <p><u>(4) Results are from Table 3 in Kok et al. (2021)</u></p> <p><u>(5) Results from Obiso et al. (2023).</u></p>					

Deleted: 2

Deleted: (1) Results based on 15 global aerosol models within the AeroCom project (Huneceus et al., 2011). (2)

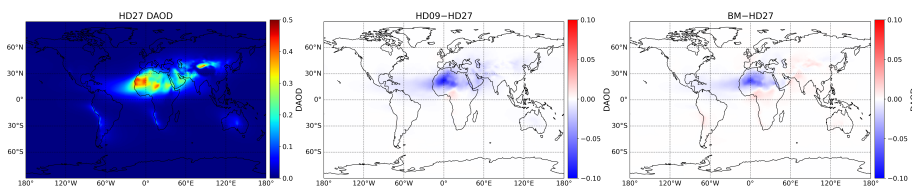
506

507 The lowest SSA of HD27 in Table 3 suggests that HD27 dust, which has been used in the standard  
508 AM4.0 model, is the most absorptive among all experiments. The HD09 dust is much less  
509 absorptive, attributed to its smaller hematite content, as indicated by the lower imaginary part of  
510 RI in the visible range (Figure 1). For the three mineral-resolved experiments, the lower global  
511 mean SSA ( $\overline{SSA}$ ), in VOL suggests that VOL-mixing dust is more absorptive than MG-mixing  
512 and BM-mixing dust. This finding is consistent with previous studies that have suggested that  
513 VOL-mixing method, when applied to minerals to compute the bulk aerosol optical properties,  
514 may artificially enhance absorption relative to scattering and lead to a lower SSA for bulk dust  
515 aerosol (Zhang et al., 2015). We can see that the global mean SSA ( $\overline{SSA}$ ) of HD09 dust is  
516 comparable to the values obtained in cases where minerals are resolved (e.g., MG and BM). This  
517 implies that, from a global perspective, HD09 dust is as absorptive as mineral-resolved dust (e.g.,  
518 MG and BM).

Moved (insertion) [2]

519 In addition to the globally averaged dust properties listed in Table 3, we illustrate the distribution  
520 of global dust mass across 5 size bins (Figure S3 in the Supplement) and the global distribution of  
521 DAOD (Figure 2) for the three experiments: before (e.g., HM27 and HD09) and after (e.g., BM)  
522 resolving mineralogy. The global dust mass distribution across the 5 size bins remains largely  
523 unchanged across experiments. Besides the subtle difference (~10%) in global mean DAOD across

528 the three experiments as listed in Table 3, the global distribution of DAOD responds differently in  
 529 HD09 and BM. Compared to HD27, reducing hematite content to HD09 generally decreases  
 530 DAOD, except over the Sahel region. In contrast, resolving mineralogy as in BM decreases DAOD  
 531 over the Sahara region while increasing DAOD over the Sahel and Asia regions. The reduction in  
 532 DAOD over the Sahara region further contributes to the decrease in dust absorption over the region,  
 533 primarily attributed to the change in dust optical properties, such as the enhancement in dust SSA.  
 534 The indistinct variation in DAOD across different experiments results from the feedback of dust  
 535 interactions with radiation (Miller et al., 2004; Pérez et al., 2006; Miller et al., 2014), which is  
 536 influenced by the distinct scattering properties of dust aerosols in each experiment as shown in  
 537 Table 3.



538  
 539 **Figure 2.** The global distribution of dust optical depth (DAOD) for HD27, and the difference in DAOD  
 540 between HD09 and BM compared to HD27. The global mean DAOD values ( $\overline{DAOD}$ ) of each experiment  
 541 are shown in Table 3.

## 542 4.2 Comparison of dust optical properties with observations

543 Iron oxides content of dust determines shortwave radiation absorption by dust: the higher amount  
 544 of iron oxides, the lower the SSA. Following our calculations of dust optical properties in Section  
 545 4.1, we compared GFDL AM4.0 modeled dust SSA (averaged in the visible band 0.44-0.625  $\mu\text{m}$ )  
 546 against AERONET SSA retrievals (averaged at two visible wavelength: 0.44  $\mu\text{m}$  and 0.67  $\mu\text{m}$ ) in  
 547 Section 4.2.1 and laboratory measurements of SSA (at 0.55  $\mu\text{m}$ ) in Section 4.2.2. The modeled  
 548 dust SSA is evaluated against observation-based results utilizing the following evaluation metrics:  
 549 the mean SSA (mSSA) is calculated based on SSA for all locations displayed in Figure 3, the  
 550 standard deviation ( $\sigma$ ), derived from SSA for all locations displayed in Figure 3, is used as an  
 551 indicator of dust SSA spatial variation; the normalized mean bias ( $nMB$ ) and normalized root  
 552 mean square error ( $nRMSE$ ) are utilized to assess the mean bias and root mean square error,  
 553 respectively, of modeled SSA in comparison to observed SSA. Definitions of  $nMB$  and  $nRMSE$   
 554 are provided in Section S3 in the Supplement.

Moved (insertion) [1]

Moved (insertion) [3]

Deleted: with

Deleted: three

Deleted: The

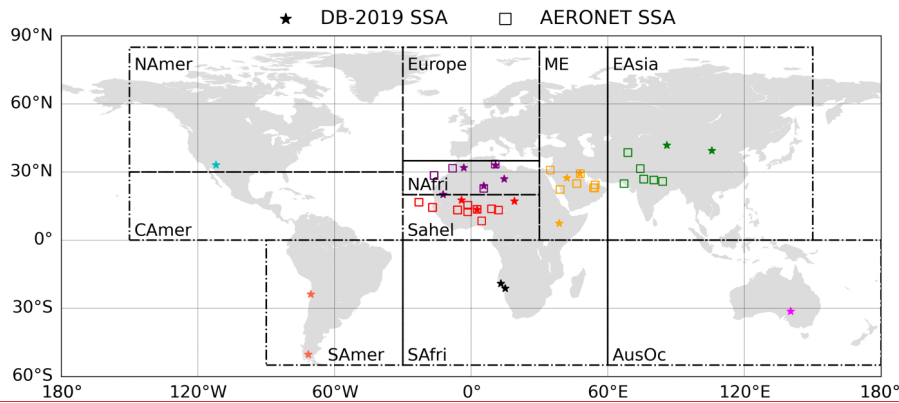
Deleted: Figure 2

Deleted: . The

Deleted: S2



561 4.2.1 Comparison with AERONET retrievals



562

563 Figure 3. Dust sample locations in Di Biagio et al. (2019) and AERONET stations selected by filtering dust  
 564 events. AERONET stations for SSA retrievals are in North Africa (NAfri), Sahel, the Middle East (ME)  
 565 and East Asia (EAsia). Lab measurements by Di Biagio et al. (2017, 2019) expand dust sampling to include  
 566 soils from North America (NAmer), South America (SAmer), South Africa (SAfri), Australia (AusOc).

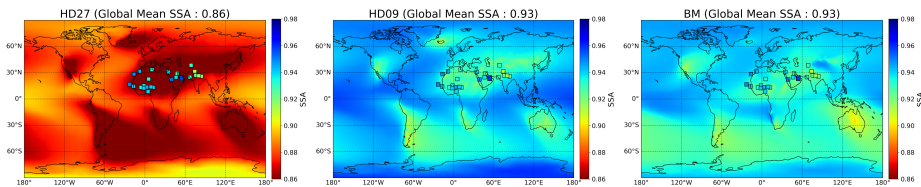
Moved (insertion) [4]

Moved (insertion) [5]

567 Figure 3 displays the AERONET stations selected by filtering dust events. The global distribution  
 568 of modeled dust SSA and AERONET retrieved SSA over the selected AERONET sites are shown  
 569 in Figure 4. There is a significant decrease in dust absorption from HD27 to HD09 globally due to  
 570 the reduction in hematite content. HD09 and BM exhibit similar dust absorption on a global scale  
 571 (e.g., the same global mean SSA), but the regional differences are evident. For instance, compared  
 572 to HD09, resolving mineralogy (e.g., BM) decreases dust absorption over Iceland and Taklamakan  
 573 regions, while enhances dust absorption over Southern Hemisphere, particularly over Australia.  
 574 Additionally, there is a shift in dust absorption from the Sahara to the Sahel region after resolving  
 575 mineralogy.

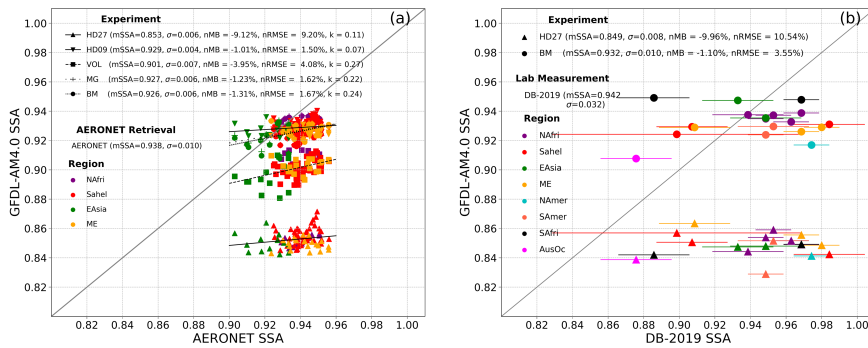
Deleted: Figure 2

576



577 Figure 4. The 19-year (2001-2019) annual mean dust SSA simulated by AM4.0 across the three experiments.  
 578 The squares represent 21-year (2000-2020) annual mean AERONET retrieved dust SSA over the selected  
 579 AERONET sites.

Moved (insertion) [6]



581

582 Figure 5. GFDL AM4.0 modeled 19-year (2001-2019) averaged monthly dust SSA (average in 0.44-0.625  
 583  $\mu\text{m}$ ) versus (a) AERONET 21-year (2000-2020) averaged monthly SSA retrievals (average at two visible  
 584 wavelengths: 0.44  $\mu\text{m}$  and 0.67  $\mu\text{m}$ ) and (b) laboratory SSA measurements (at 0.55  $\mu\text{m}$ ) of dust particles  
 585 with diameter ranging from 0.2  $\mu\text{m}$  up to 10  $\mu\text{m}$  obtained by Di Biagio et al. (2019) (DB-2019). The lab  
 586 measurements were carried out in March 2015, horizontal error bars represent measurement uncertainties.  
 587 Markers represent different experiments, and colors represent different regions. mSSA in the legend  
 588 represents the mean SSA averaged over all locations indicated in Figure 2 (squares for AERONET, stars  
 589 for DB-2019). The standard deviation ( $\sigma$ ), normalized mean bias (nMB), normalized root mean square error  
 590 (nRMSE), and the slope of linear regression ( $k$ ) are also indicated in the legend.

591 Figure 5a shows GFDL AM4.0 modeled 19-year (2001-2019) averaged dust SSA (average in 0.44-  
 592 0.625  $\mu\text{m}$ ) versus AERONET SSA (average at 0.44  $\mu\text{m}$  and 0.67  $\mu\text{m}$ ) retrievals. Compared to  
 593 AERONET SSA retrievals, both HD27 and VOL overestimate dust absorption, as indicated by  
 594 their relatively low SSA (Figure 5a). HD27 dust is the most absorptive, indicating that the standard  
 595 AM4.0 dust is overly absorptive. Dust SSA in MG and BM are quite similar (i.e., mSSA: 0.926  
 596 versus 0.927) and show a better agreement with AERONET measurements ( $nMB \approx -1.3\%$  and  
 597  $nRMSE \approx 1.6\%$ ), and they exhibit stronger scattering (i.e., higher SSA) than HD27 and VOL.  
 598 HD09 is almost as scattering as MG and BM, as indicated by the mSSA of 0.929 versus 0.926 and  
 599 0.927 in Figure 5a, which is consistent with the global mean SSA (SSA) results shown in Table 3.  
 600 Overall, both the fixed mineralogy dust HD09 and mineral-resolved MG and BM dust agree well  
 601 with AERONET SSA retrievals, while HD27 and VOL are too absorptive. Therefore, we  
 602 recommend using mixing ratios of MG or BM in calculating optical properties of internal mixture  
 603 of hematite and clay minerals. Unless otherwise specified, in the following part of the paper, we  
 604 will refer to mineral-resolved experiments as MG or BM.

Moved (insertion) [7]

Moved (insertion) [8]

Moved (insertion) [9]

Deleted: Figure 3

Deleted: Figure 3a).

Deleted: mean SSA

Deleted: mean SSA

Deleted: Figure 3

Deleted: Table 3

611 We further assess the SSA spatial variation (indicated by  $\sigma$ ) for each experiment from AM4.0 by  
612 comparing it to observation-based results. SSA is generally determined by dust mineralogy, size  
613 as well as shape. ~~Various~~ dust mineralogy leads to distinct dust SSA due to the different absorption  
614 properties of minerals (Figure 1). Coarser dust generally tends to be more absorptive (i.e., has  
615 lower SSA) than finer dust when other factors are the same (Ryder et al., 2018). Spherical dust  
616 assumption tends to underestimate dust SSA (Huang et al., 2023). Given the uncertainty in dust  
617 shape, we assume dust particles to be spherical in this study, aligning with other model studies  
618 ~~(e.g., Gliß et al., 2021)~~. Consequently, in the mineral-resolved experiments of this study, namely  
619 VOL, MG, and BM, dust mineralogy and dust size are the two factors affecting the SSA spatial  
620 variation.

Deleted: various

621 Conversely, in homogeneous dust experiments, specifically HD27 and HD09, SSA variation is  
622 solely attributed to variation in dust size, as dust mineralogy remains uniform globally.  
623 Interestingly, HD09 demonstrates smaller spatial variation (i.e., lower  $\sigma$ ) in SSA compared to  
624 HD27 (Figure 5a). To investigate the impact of dust size on SSA for different hematite content  
625 (e.g., HD27 and HD09), we perform a simple test in Section S4 of the Supplement. Supplementary  
626 Figure S4 and S5 illustrate that the variation of SSA due to the dust particle size is more  
627 pronounced with increasing absorption, i.e., from HD09 to HD27. This suggests that enhancement  
628 in dust scattering relative to dust absorption (i.e., an increase in SSA) mitigates the sensitivity of  
629 SSA to dust size.

Deleted: (e.g. Gliß et al., 2021)

Deleted: Figure 3a).

Deleted: S3

Deleted: S3 illustrates

630 The conclusions above provide an understanding of the SSA spatial variation (indicated by  $\sigma$ )  
631 before (i.e., HD27 and HD09) and after (i.e., VOL, MG, and BM) implementing dust mineralogy.  
632 The same  $\sigma$  (0.06) between HD27 and BM can be explained as follows: Because mineral-resolved  
633 BM-mixing dust is overall more scattering than HD27 dust, resulting in a reduced sensitivity of  
634 SSA to size, therefore, the  $\sigma$  of SSA caused by dust size is reduced in BM relative to HD27.  
635 However, the incorporation of dust mineralogy in BM leads to an increase of  $\sigma$ . These contrasting  
636 effects compensate for each other, resulting in the same  $\sigma$ . In contrast, HD09 is overall as  
637 scattering as BM, as shown in Table 3 and Figure 5a, suggesting a similar sensitivity of SSA to  
638 size. Therefore, the ~~incorporation of dust mineralogy in BM results in a higher  $\sigma$  compared to~~  
639 HD09. ~~Overall, while the enhancement in  $\sigma$  can be offset by the reduction in  $\sigma$  due to the reduced~~

Deleted: Table 3

Deleted: Figure 3

Deleted: in BM relative

Deleted: is attributed to

Deleted: incorporation of dust mineralogy.

650 sensitivity to dust size, resolving dust mineralogy increases  $\sigma$  on its own, consequently enhancing  
651 the spatial variation in dust SSA.

652 Worth to mention, AERONET dust is quite scattering as shown in Figure 5a, therefore its SSA is  
653 less sensitive to dust size. The high  $\sigma$  (0.010) of AERONET SSA can be mainly due to spatial  
654 variations in dust mineral composition. Reducing dust hematite content (HD09) leads to a better  
655 agreement in mean SSA with AERONET (i.e., more scattering dust) but results in very low  $\sigma$   
656 (0.004), while implementing dust mineralogy (e.g., MG and BM) retains the agreement with  
657 AERONET in mean SSA and, at the same time, increases  $\sigma$  (0.006).

658 Besides the standard deviation ( $\sigma$ ), the slopes ( $k$ ) obtained from the statistics of modeled SSA  
659 versus AERONET SSA can also indicate the regional contrast of SSA. The regional contrast of  
660 AERONET SSA is well captured by the model when  $k$  is one, underestimated when  $k$  is lower than  
661 one, and overestimated when  $k$  is higher than one. As such, the slopes in Figure 5a show that the  
662 contrast in SSA from different regions (e.g., North Africa vs. East Asia) observed by AERONET  
663 is better captured by mineral-resolved experiments (e.g., VOL, MG and BM with  $k$  ranging from  
664 0.22 to 0.27) than homogeneous dust experiments (e.g., HD27 and HD09 with  $k$  ranging from 0.07  
665 to 0.11). However, the modeled regional contrast of SSA in mineral-resolved experiments remains  
666 overly underestimated (i.e.,  $k$  is much lower than one). The significant underestimation of regional  
667 SSA contrast ( $k$  and spatial variation ( $\sigma$ ) in AM4.0, even after accounting for mineralogy, implies  
668 that something important is still missing in models. For instance: 1) the observed regional contrast  
669 in iron oxides content may be higher than that in the soil map used in this study, and 2) the model  
670 may have underestimated regional contrasts in the dust aerosol size distribution and thus their  
671 contribution to SSA, and 3) spatial variation of dust shape, which is not taken into account in the  
672 model.

#### 673 4.2.2 Comparison with laboratory measurements

674 We further compare the GFDL AM4.0 modeled dust SSA (average in 0.44-0.625  $\mu\text{m}$ ) with DB-  
675 2019 laboratory measurements of SSA at 0.55 $\mu\text{m}$  (Figure 5b). Figure 3 shows the locations where  
676 dust samples were collected for the lab measurements. Considering that MG and BM are very  
677 similar in terms of dust absorption and agree the best with AERONET SSA, we select BM as a  
678 representative to compare with DB-2019 SSA. Moreover, to evaluate how dust absorption is  
679 represented in the standard AM4.0 relative to lab measurements, we also show the comparison of

Deleted: Figure 3

Deleted: is

Deleted: Overall, reducing

Deleted: Figure 3

Deleted: suggests

Deleted: need for a higher

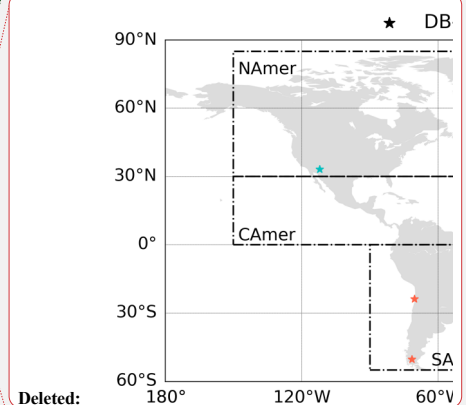
Moved up [3]: Figure 2.

Moved up [5]: Dust sample locations in Di Biagio et al. (2019) and AERONET stations selected by filtering dust events. AERONET stations for SSA retrievals are in North Africa (NAfri), Sahel, the Middle East (ME) and East Asia (EAsia). Lab measurements by Di Biagio et al. (2017, 2019) expand dust sampling to include soils from North America (NAmer), South America (SAmer), South Africa (SAfri), Australia (AusOc).

Moved up [4]: Figure 3.

Moved up [8]: GFDL AM4.0 modeled 19-year (2001-2019) averaged monthly dust SSA (average in 0.44-0.625  $\mu\text{m}$ ) versus (a) AERONET 21-year (2000-2020) averaged monthly SSA retrievals (average at two visible wavelengths: 0.44  $\mu\text{m}$  and 0.67  $\mu\text{m}$ ) and (b) laboratory SSA measurements (at 0.55  $\mu\text{m}$ ) of dust particles with diameter ranging from 0.2  $\mu\text{m}$  up to 10 $\mu\text{m}$  obtained by Di Biagio et al. (2019) (DB-2019). The lab measurements were carried out in March 2015, horizontal error bars represent measurement uncertainties. Markers represent different experiments, and colors represent different regions. mSSA in the legend

Moved up [9]: The standard deviation ( $\sigma$ ), normalized mean bias (nMB), normalized root mean square error (nRMSE),



Deleted: 180° 120°W 60°V

Deleted: ... [1]

Deleted: Figure 2 (squares for AERONET, stars for DB-2019). ...

Deleted: Figure 3b). Figure 2

734 SSA between HD27 used in the standard AM4.0 and DB-2019 (Figure 5b). Consistent with the  
735 comparison with AERONET, the comparison with lab measurements suggests that dust  
736 representation in the standard AM4.0 (i.e., HD27) is excessively absorptive. The smaller nMB and  
737 nRMSE values in BM suggests that SSA of BM agrees better with lab measurements.

Deleted: Figure 3b).

738 Moreover, regarding spatial variation ( $\sigma$ ), resolving dust mineralogy in BM increases  $\sigma$  from 0.008  
739 for HD27 to 0.010 for BM, even though it is still lower than the  $\sigma$  (0.032) in DB-2019 lab  
740 measurements. Note that the variation for HD27 results from the high sensitivity of SSA to dust  
741 size due to its higher absorption (as discussed in Supplementary Section S4). The inability to  
742 reproduce spatial variation observed in the lab measurements is likely attributed to two aspects.  
743 The first limitation is the fact that samples of DB-2019 are from soils rather than aeolian dust.  
744 Aeolian dust is expected to exhibit greater uniformity in mineralogy than soils because of the  
745 atmospheric mixing of dust emitted from various soil sources. The second one is associated with  
746 the under-representation of regional contrast in iron oxides content in our model. Observations  
747 from the EMIT are therefore essential to constrain soil mineralogy in climate models.

Deleted: S3

## 748 5 Impacts of dust mineralogy on climate

749 Resolving dust mineralogy in climate models affects dust optical properties (as discussed in  
750 Section 4) and their spatial and temporal variability, thereby affecting their interactions with  
751 shortwave (SW) and longwave (LW) radiation. The variability in dust radiative interactions further  
752 induces the fast response of land surface temperature, circulation, and precipitation. To investigate  
753 the impacts of resolving dust mineralogy on climate, we need to compare modeled results in  
754 mineral-resolved experiments to the baseline homogeneous dust (i.e., non-resolved mineralogy)  
755 control run. As a result, the significance of the impacts depends on the selection of the baseline  
756 homogeneous dust experiment. In this section, we investigate the impacts of resolving dust  
757 mineralogy compared to two baseline homogeneous dust experiments. One baseline experiment is  
758 the homogeneous dust used in the standard GFDL AM4.0, in which dust mineralogy is assumed  
759 to be temporally and spatially uniform (i.e., non-resolved), with a volume fraction of 2.7%  
760 hematite (HD27). The impacts of resolving dust mineralogy, compared to the baseline HD27, can  
761 be attributed to two factors: 1) the reduction in dust absorption after resolving dust mineralogy in  
762 comparison to HD27 as discussed in Section 4, and 2) spatial and temporal variations in dust  
763 scattering properties induced by inhomogeneity in dust mineralogy. The other baseline experiment

Deleted: , which are investigated

Deleted: . To understand the impacts of dust minerals on climate, we proceed in two steps. Firstly

Deleted: on radiation and climate relative to the HD27 control run. The HD27 control run represents

Deleted: model

Deleted: ,

Deleted: . This step explores the influence

Deleted: on climate

Deleted: the standard AM4.0 model. Secondly, we go beyond the representation of dust aerosols

Deleted: the standard AM4.0 model by replacing our homogeneous dust in

Deleted: control run with more scattering homogeneous dust (i.e., HD09) to assess the impacts of resolving

Deleted: of dust mineralogy on climate relative to the

782 is the homogeneous dust, with a volume fraction of 0.9% hematite (HD09). Given the comparable  
783 global mean dust scattering properties (e.g., SSA) between the control run HD09 and mineral-  
784 resolved experiments (e.g., MG and BM), the impacts of resolving dust mineralogy, compared to  
785 baseline HD09, is solely attributed to the inhomogeneity in dust scattering properties induced by  
786 resolving dust mineralogy.

## 787 5.1 Impacts on Clear-sky Radiative Fluxes

788 We start our analysis by examining the impacts of resolving dust mineralogy on clear-sky radiative  
789 fluxes. By ‘clear-sky’, we mean that our results do not consider the radiative effects of clouds. We  
790 use anomalies ( $\Delta F$ ) to evaluate the impacts of resolving mineralogy on clear-sky radiative fluxes,  
791 which is defined as,  $\Delta F = F_1^\uparrow - F_2^\uparrow$ , where  $F_1^\uparrow$  is the 19-year mean clear-sky upward radiative  
792 fluxes with resolved mineralogy,  $F_2^\uparrow$  is the 19-year mean clear-sky upward radiative fluxes for  
793 homogeneous dust. Section S5 in the Supplement provides the clear-sky radiative fluxes anomalies  
794 at TOA and surface (SFC) induced by resolving dust mineralogy over the global scale, we see  
795 much more significant anomalies over the North Africa than other regions, which makes senses  
796 because that dust aerosol is the most dominant aerosol species in this area. The changes in dust  
797 aerosol optical properties have a greater potential to lead to significant impacts on radiation and  
798 climate over the region than in the others. Therefore, this section focuses on the North Africa  
799 region, where the Sahara Desert, the largest dust source in the world, is located. The Sahara (20°N-  
800 30°N, 10°W-35°E) and the Sahel (10°N-20°N, 10°W-35°E) regions are studied separately. We  
801 specifically analyze the results for the June-July-August (JJA) season when dust loading is at its  
802 highest and the West African Monsoon is the strongest.

### 803 5.1.1 Impacts on Clear-sky Radiative Fluxes relative to HD27

804 Before comparing mineral-resolved experiments (e.g., BM) with HD27 control run, the dust has  
805 been used in the standard GFDL AM4.0, to understand their impacts on clear-sky radiative fluxes  
806 relative to HD27, it’s worth recapping that the effects of resolving mineralogy relative to HD27  
807 can be attributed to two factors: the reduction in dust absorption and the variation in dust scattering  
808 properties induced by the mineralogical inhomogeneity.

Deleted: experiment. As shown in Table 3

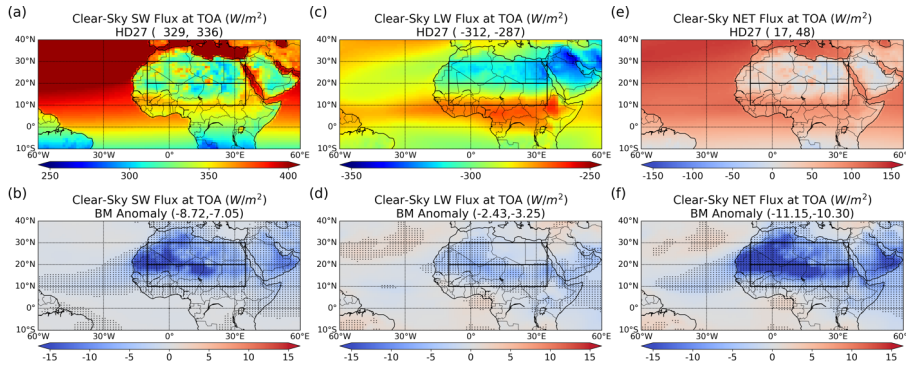
Deleted: Figure 3a,

Deleted: is much more scattering than HD27 and approximately as ...

Deleted: as the mineral-resolved dust (i.e., MG-mixing, and BM-mixing dust) in terms of globally averaged SSA. Therefore, this step sheds light on the impacts of resolving dust mineralogy on climate given similar globally averaged scattering properties with and without resolved

Deleted: Section S4

Deleted: . Therefore, our study



820

821 Figure 6. Seasonal mean JJA climatology (2001-2019) clear-sky SW (1<sup>st</sup> column), LW (2<sup>nd</sup> column) and  
 822 Net (3<sup>rd</sup> column) radiative flux at TOA for the HD27 control run (1<sup>st</sup> row) and their anomalies resulting  
 823 from resolving dust mineralogy in Bruggeman-mixing experiment (2<sup>nd</sup> row). Downward direction is defined  
 824 as positive. The dotted area denotes anomalies that are statistically significant. The two values in  
 825 parentheses within the title of each figure are domain average for the Sahara and Sahel regions.

826 The first row in Figure 6 illustrates the modeled clear-sky shortwave (SW), longwave (LW) and  
 827 net (NET: the combination of SW and LW) radiative flux at TOA from the HD27 control run.  
 828 Relative to HD27, mineral-resolved dust (e.g., BM-mixing dust) generally reflects more SW  
 829 radiation back to space and induces negative SW flux anomalies at TOA (Figure 6a, b; Positive:  
 830 downward). Relative to the HD27 control run, the LW flux anomaly at TOA resulting from  
 831 resolving mineralogy is less substantial compared to SW flux anomaly (Figure 6c, d). After  
 832 combining both SW and LW, resolving mineralogy turns out to induce substantial decrease in NET  
 833 flux at TOA, with a more than 50% negative anomaly over the Sahara and around a 20% negative  
 834 anomaly over the Sahel (see values in parentheses in Figure 6e, f). Therefore, less NET radiation  
 835 reaches the Earth at TOA in the mineral-resolved dust cases due to their lower absorptivity.

Moved (insertion) [10]

Moved (insertion) [11]

Deleted: column

Deleted: Figure 4

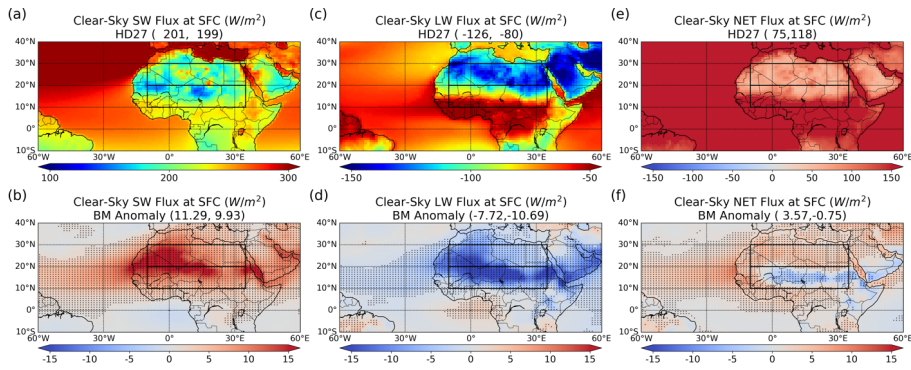
Deleted: i.

Deleted: ., VOL-mixing, MG-mixing, and

Deleted: Figure 4 a-d; Positive: downward). In addition, MG-mixing and BM-mixing dust induce stronger reflection anomalies than VOL-mixing dust. The results are consistent with the fact that mineral-resolved dust is less absorptive than HD27 dust in the visible spectrum, and MG-mixing and BM-mixing dust are even less absorptive than VOL-mixing dust, as discussed in Section 4.

Deleted: Figure 4 e-h).

Deleted: Figure 4 i-l).



849

850 Figure 7. As in Figure 6, but for the surface.

851 At the surface (SFC) in [Figure 7](#), the enhanced scattering of mineral-resolved dust scatters more  
 852 SW radiation toward Earth's surface, leading to a positive SW flux anomaly at SFC (Positive:  
 853 downward). In the LW, the cooling of the mineral-resolved dust layer, due to its low absorption,  
 854 results in less LW radiation being emitted toward Earth's surface. This reduction in the downward  
 855 LW emission outweighs the change in the upward LW emission from the Earth's surface, thereby  
 856 causing a negative LW flux anomaly at SFC. The positive anomalies in SW radiation are  
 857 approximately canceled out by the negative anomalies in LW radiation ([Figure 7](#)). As a result, a  
 858 similar amount of radiation reaches the Earth's surface in both HD27 and mineral-resolved cases.  
 859 Despite less NET radiation entering the Earth at TOA in mineral-resolved cases, the similar  
 860 amount of NET radiation reaching the Earth's surface indicates that less NET radiation is absorbed  
 861 in the atmosphere in mineral-resolved cases.

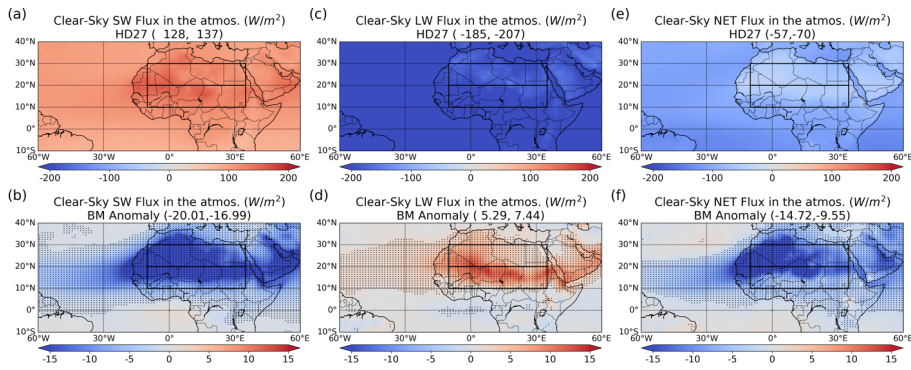
Moved (insertion) [12]

Deleted: Figure 5

Deleted: ,

Deleted: Figure 5).





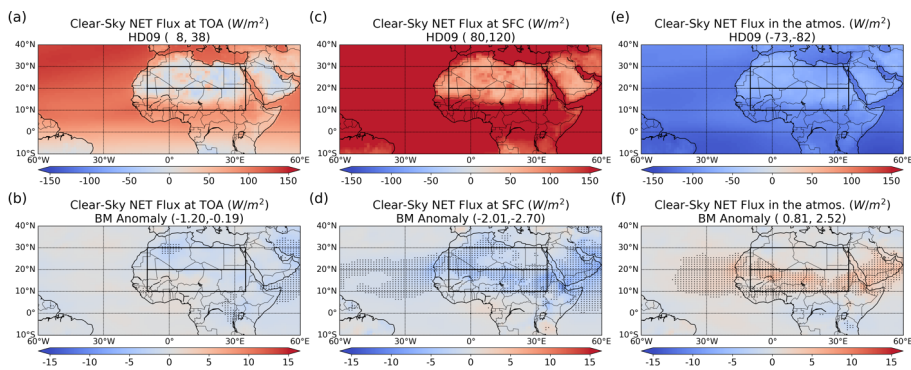
865

866 Figure 8. As in the Figure 6, but for the radiative flux absorbed in the atmosphere.

867 In Figure 8, the negative SW flux anomalies are partially offset by positive LW flux anomalies,  
 868 resulting in negative NET flux anomalies in the atmosphere. These anomalies amount to  
 869 approximately a 25% reduction over the Sahara and 10% reduction over the Sahel (see values in  
 870 parentheses in Figure 8b, d, f).

871 5.1.2 Impacts on Clear-sky Radiative Fluxes relative to HD09

872 Before comparing mineral-resolved experiments with HD09 control run, where the homogeneous  
 873 dust is as absorptive as mineral-resolved dust (e.g., MG and BM) from a global perspective, to  
 874 understand their impacts on clear-sky radiative fluxes relative to HD09, it's worth recapping that  
 875 the effects of resolving mineralogy relative to HD09 are primarily attributed to the variation in  
 876 dust scattering properties induced by the mineralogical inhomogeneity.



877

Moved (insertion) [13]  
 Deleted: As shown in Figure 6

Deleted: Figure 6 i-l

880 Figure 9. As in the Figure 6, but for HD09 control run. In addition, SW and LW flux anomalies are not  
881 shown here. Clear-sky net flux at TOA (1<sup>st</sup> column), at surface (2<sup>nd</sup> column), and in the atmosphere (3<sup>rd</sup>  
882 column) are shown in this figure.

883 Figure 9 shows the clear-sky fluxes anomalies with respect to HD09 over North Africa, the  
884 anomalies over the global scale are shown in Figure S7, S9, S11 and S13 in the Supplement.

885 In contrast to the anomalies with respect to HD27 control run, resolving dust mineralogy does not  
886 cause substantial anomalies (< 5%) in clear-sky fluxes with respect to HD09 control run. This can  
887 be attributed to their similarity in dust scattering properties from a global mean perspective,  
888 particularly SSA as shown in Figure 5. The comparable effects of HD09 and mineral-resolved dust  
889 on radiation suggest that resolving dust mineralogy does not have significant impacts on clear-sky  
890 fluxes when homogeneous dust is as scattering as mineral-resolved dust aerosols on a global scale.

891 However, the equivalence between HD09 and mineral-resolved dust in terms of their interactions  
892 with radiation may be related to the three limitations in the current model simulations: 1) Soil  
893 mineralogy: The limited soil mineralogy database fails to adequately capture the regional variation  
894 of iron content (or SSA) within the region; 2) Dust emission based on Ginoux et al. (2001) uses a  
895 continuous function of topography, which does not take into account geomorphological  
896 characteristics of the surface to differentiate soil properties of dust sources as done by others  
897 (Zender et al., 2003; Bullard et al., 2011); 3) Dust transport: Excessive numerical diffusion may  
898 occur when solving advection equation (Ginoux, 2003). Given all those limitations of our model  
899 simulations, this finding may differ with improved representation of dust sources and transport.  
900 Such improvement may come from spaceborne soil mineralogy dataset (e.g., EMIT) that may  
901 capture accurately the regional contrasts in iron oxides content.

### 902 5.1.3 Compare Clear-sky Radiative Fluxes with CERES Observations

903 Furthermore, we conduct a comparison of modeled SW upward, LW upward, NET downward flux  
904 at TOA with observation-based results from CERES\_EBAF\_Ed4.2 product (see Table 4). The  
905 difference between modeled flux and CERES observations are listed in parentheses within the title  
906 of each figure in Table 4. Compared to HD27, the more scattering HD09 and mineral-resolved BM  
907 achieve much better agreement with CERES observations in clear-sky flux (i.e., SWup, LWup and  
908 NETdn) at TOA. This is evident in the smaller values of HD09 – CERES (e.g., NETdn: 1.6 for the  
909 Sahara and 2.4 for the Sahel) and BM – CERES (e.g., NETdn: 0.4 for the Sahara and 2.1 for the  
910 Sahel) compared to HD07 – CERES (e.g., NETdn: 11.3 for the Sahara and 12.4 for the Sahel), as

Moved (insertion) [14]

Moved (insertion) [15]

Deleted: Figure 7

Deleted: S5,

Deleted: and

Deleted: Figure 3

Deleted: regionally averaged

Deleted: . The

Deleted: Figure 8).

Deleted: Figure 8

919 shown by the values in parentheses in Table 4. Between HD09 and BM, BM tends to agree slightly  
 920 better with CERES.

921 Table 4. Comparison of modeled clear-sky SW upward (SWup, 1<sup>st</sup> row), LW upward (LWup, 2<sup>nd</sup> row) and  
 922 NET downward (NETdn, 3<sup>rd</sup> row) fluxes at TOA with CERES observation-based results over 2001-2019  
 923 JJA. The 1<sup>st</sup> column shows the clear-sky flux estimates at TOA from CERES\_EBAF\_Ed4.2 product, which  
 924 represents clear-sky flux with clouds removed from the atmospheric column. The following columns show  
 925 the difference of modeled clear-sky flux at TOA in HD27 (2<sup>nd</sup> column), HD09 (3<sup>rd</sup> column) and BM (4<sup>th</sup>  
 926 column) experiments from CERES observations. The two values in parentheses represent domain average  
 927 for the Sahara and Sahel regions, as indicated in figures in Section 5.1.2. Specifically, the first column  
 928 (CERES) is domain averaged flux, while the second (HD27 – CERES), third (HD09 – CERES), and fourth  
 929 (BM – CERES) columns are domain averaged flux differences between model and CERES observation-  
 930 based results.

	CERES	HD27 – CERES	HD09 – CERES	BM – CERES
Clr SWup flux at TOA (W/m <sup>2</sup> )	(135, 113)	(-9.3, -9.4)	(-1.1, -2.2)	(-0.6, -2.3)
Clr LWup flux at TOA (W/m <sup>2</sup> )	(314, 291)	(-1.4, -3.1)	(-0.6, -0.5)	(0.2, -0.1)
Clr NETdn flux at TOA (W/m <sup>2</sup> )	(6, 36)	(11.3, 12.4)	(1.6, 2.4)	(0.4, 2.1)

931

## 932 5.2 Impacts on land temperature

933 Here we explore the impacts on the temperature vertical profile and near-land surface temperature,  
 934 relative to HD27 and HD09, respectively. Compared to the HD27 control run, lower absorption of  
 935 radiation in the atmosphere by mineral-resolved dust aerosols results in statistically significant  
 936 negative temperature anomalies in the atmosphere ranging from 800 mb up to 500 mb where dust  
 937 aerosols are mainly located (Figure 10). In contrast, there is no statistically significant temperature  
 938 anomaly for mineral-resolved dust cases compared to HD09, as illustrated by the red curves in  
 939 Figure 10 This finding aligns with the insubstantial anomalies (<5%) in clear-sky NET radiative  
 940 fluxes discussed in Section 5.1.2. In the subsequent part of the section, we will delve into  
 941 comparing mineral-resolved experiment (using BM as an example) with the HD27 control run.  
 942 This comparison will help us further understand the impact of dust aerosols with distinct  
 943 absorption on land temperature.

Deleted: Figure 8.

Moved up [6]: Figure 4.

Moved up [11]: Downward direction is defined as positive. The dotted area denotes anomalies that are statistically significant. The two values in parentheses within the title of

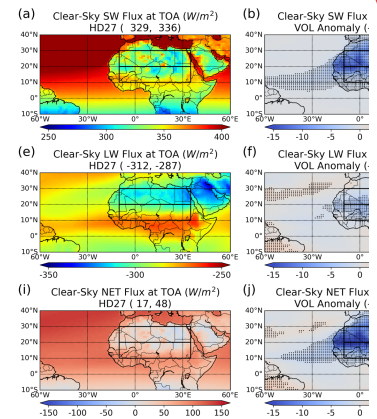
Moved up [7]: Figure 5.

Moved up [10]: Figure 6.

Moved up [12]: Figure 7.

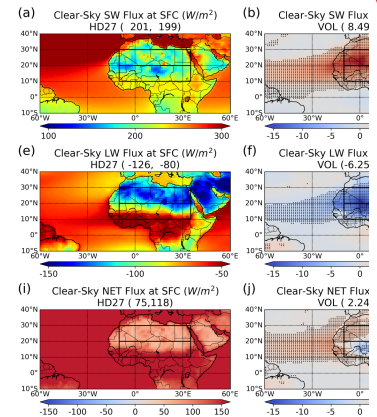
Moved up [15]: In addition, SW and LW flux anomalies are not shown here.

Moved up [13]: Figure 8.



Deleted:

Deleted: Seasonal mean JJA climatology (2001-2019) clear-sky SW (1<sup>st</sup> row), LW (2<sup>nd</sup> row) and Net (3<sup>rd</sup> row) radiative flux at TOA for the HD27 control run (1<sup>st</sup> column) and ... [2]



Deleted:

Deleted: As in Figure 4, but for the surface. [3]

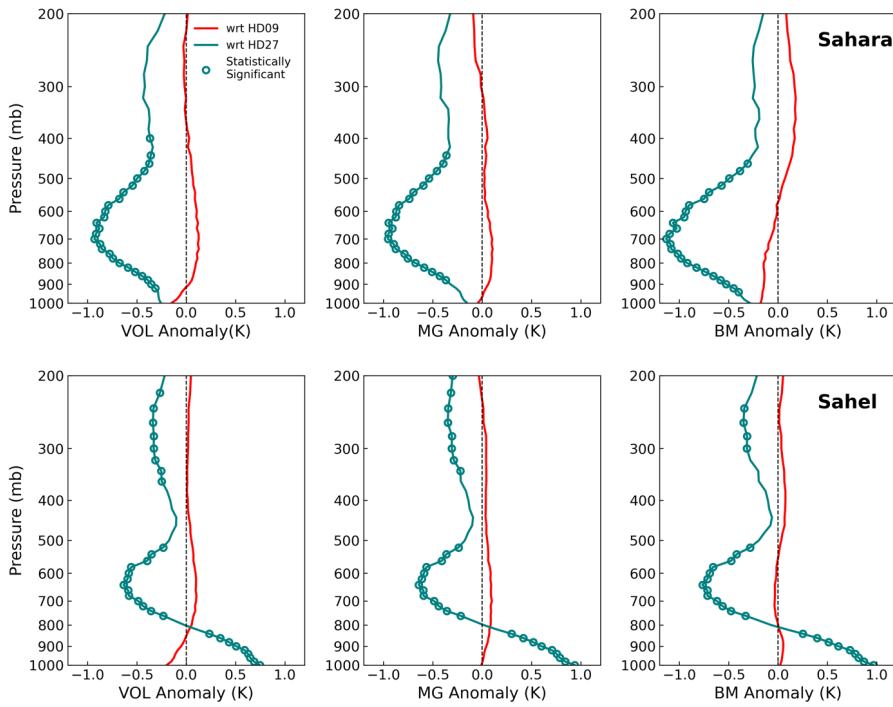
Deleted: As in the Figure 4, but for the radiative flux absorbed in the atmosphere. [4]

Deleted: As in the Figure 4, but for HD09 control run.

Deleted: Clear-sky net flux at TOA (1<sup>st</sup> row), at surface (2<sup>nd</sup> row), and in the atmosphere (3<sup>rd</sup> row) are shown in this figure. [5]

Deleted: within the title of each figure are...represent domain average for the Sahara and Sahel regions. [6]

Deleted: ....relative to HD27 and HD09, respectively. Compared to the HD27 control run, lower absorption of radiation in the atmosphere by mineral-resolved dust [7]

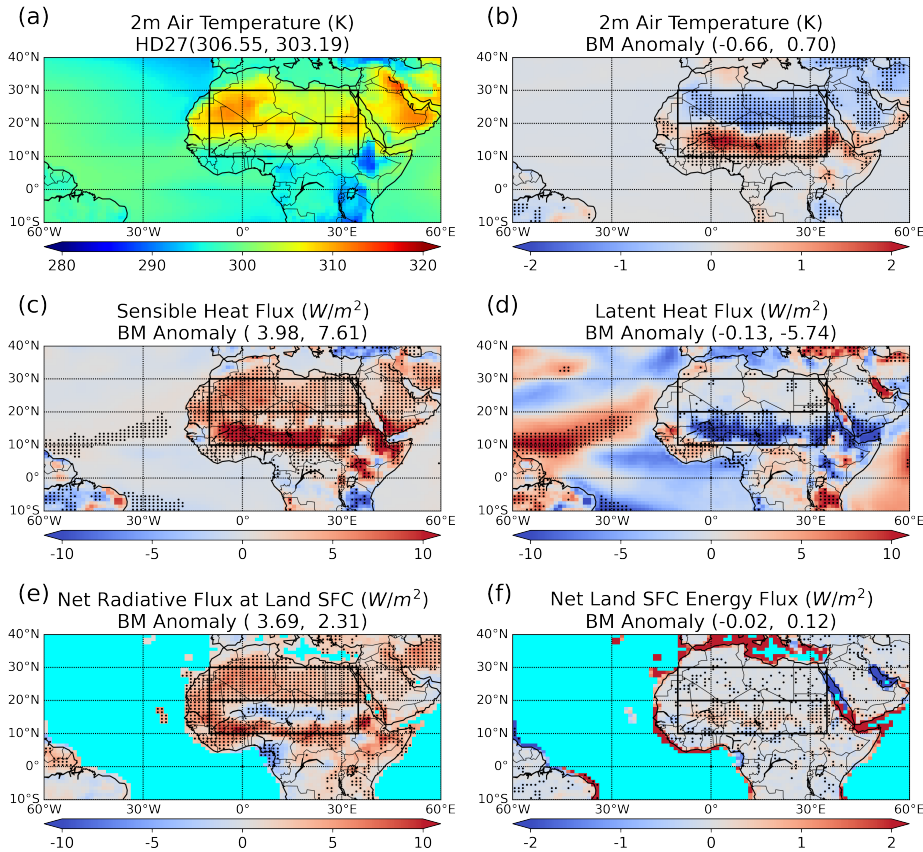


Deleted: Figure 10

1061

1062 Figure 10. Vertical profile of temperature anomaly induced by resolving dust mineralogy for the Sahara (1<sup>st</sup>  
 1063 row) and the Sahel (2<sup>nd</sup> row) regions in the three mineral-resolved experiments (i.e., VOL, MG, BM). Green  
 1064 lines represent temperature anomalies with respect to HD27 control run. Red lines are temperature  
 1065 anomalies with respect to HD09 control run. The circles represent statistically significant temperature  
 1066 anomaly.

Moved (insertion) [16]



1068

1069 Figure 11. Air temperature at 2-meter from HD27 control run (a), anomaly (b) induced by implementing  
 1070 Bruggeman-mixing minerals in BM experiment, surface sensible heat flux (c), latent heat flux (d), net  
 1071 radiative flux (e), net energy flux (f) anomalies between BM and HD27; Upward flux is positive in (c) and  
 1072 (d), while downward flux is positive in (e) and (f). Net energy flux (f) is the subtraction of (c), (d), and  
 1073 downward ground flux from (e). Note that ground flux is not shown in the figure considering its relatively  
 1074 small magnitude, but it is included in the land surface net energy flux calculations in subplot (f). The dotted  
 1075 area denotes anomalies that are statistically significant. The two values in parentheses within the title of  
 1076 each figure are domain average for the Sahara and Sahel regions.

1077 Figure 11a shows air temperature at 2-meter from HD27 control run over the Northern Africa.  
 1078 Near the land surface, more scattering mineral-resolved dust induces a temperature decrease (i.e.,  
 1079 negative temperature anomaly  $-0.66$  K) over the Sahara and a temperature increase (i.e., positive

Moved (insertion) [17]

Deleted: -

1081 temperature anomaly 0.70 K) over the Sahel as shown [Figure 11b](#). To understand this phenomenon,  
 1082 we further analyze the surface energy budget in [Figure 11c-f](#).  
 1083 [Radiative flux perturbation over land is quickly equilibrated by balancing surface radiative fluxes](#)  
 1084 [with](#) sensible heat flux, latent heat flux and ground flux (i.e., downward heat flux into the ground),  
 1085 [which results in nearly zero net energy flux at land surface as shown in Figure 11f](#). Precisely, the  
 1086 radiative flux anomaly comprises two contributions: one is the instantaneous radiative forcing (IRF)  
 1087 caused by the change in dust mineralogy in the atmosphere, and the other one is the associated  
 1088 radiative feedbacks. For simplicity, we will not partition the radiative flux anomaly in our  
 1089 discussion here. [Over the Sahel region, the positive net radiative flux anomaly at land surface is](#)  
 1090 [balanced out by the increased sensible heat flux and the decreased latent heat flux as well as ground](#)  
 1091 [flux. Note that the ground flux is generally small in magnitude and not shown in Figure 11, but we](#)  
 1092 [include it in calculating net surface energy flux in Figure 11f](#). The decrease of latent heat flux over  
 1093 the Sahel in BM case ([Figure 11d](#)) is due to the depletion of soil moisture (and therefore  
 1094 evaporation) in the region as shown in [Figure 12](#). The depletion of soil moisture is caused by the  
 1095 decrease in moisture carried by onshore winds over the Sahel and the decrease in precipitation  
 1096 over the same region, as will be discussed in section 5.3. Therefore, a large enhancement of  
 1097 sensible heat flux ( $\sim 7.6 \text{ W/m}^2$ ) is needed ([Figure 11c](#)) not only to compensate for the depletion  
 1098 in latent heat flux ( $\sim 5.7 \text{ W/m}^2$  in [d](#)), but also to balance out the increased net radiative flux ( $\sim 2.3$   
 1099  $\text{W/m}^2$  in [Figure 11e](#)). As a result, higher land surface temperature with anomaly around  $0.7 \text{ K}$  is  
 1100 needed in the region to achieve the required sensible heat flux enhancement.

Deleted: Figure 10b.

Field Code Changed

Deleted: Land equilibrates energy rather

Deleted: with

Deleted: fluxes, namely the

Deleted: flux,

Deleted: ).

Deleted: So, the radiative flux anomalies at land surface are quickly equilibrated by the turbulent flux of energy through sensible heat flux, latent heat flux as well as ground flux, which results in nearly zero net energy flux at land surface as shown in Figure 10f.

Deleted: Figure 10

Deleted: Figure 10f.

Deleted: Figure 10

Deleted: Figure 11.

Deleted: 5

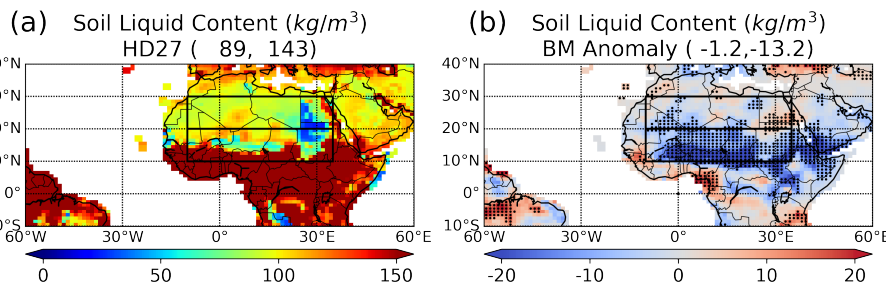
Deleted: Figure 10

Deleted: 3

Deleted: Figure 10

Deleted: Figure 10

Deleted: 6K



1101

1102 [Figure 12. Soil liquid content in HD27 control run \(a\) and anomaly resulting from implementing](#)  
 1103 [Bruggeman-mixing minerals in the BM experiment \(b\). The two values in parentheses within the title of](#)  
 1104 [each figure are domain average for the Sahara and Sahel regions.](#)

Moved (insertion) [18]

Moved (insertion) [19]

1126 Over the Sahara region, latent heat flux does not change from HD27 case to BM case, therefore,  
 1127 the increased net radiative flux ( $\sim 3.69 \text{ W/m}^2$ ) in BM compared to HD27 is mainly balanced out  
 1128 by the enhanced sensible heat flux ( $\sim 3.98 \text{ W/m}^2$ ) which requires a larger temperature gradient  
 1129 between surface and atmosphere. However, there is a very strong negative temperature anomaly  
 1130 (around  $-1\text{K}$ ) in the atmosphere near 700 hPa due to less dust absorption in BM as we discussed  
 1131 in Figure 10. The strong negative temperature anomaly in the lower atmosphere effectively  
 1132 increases the vertical temperature gradient. As such, it is not necessary for the land surface  
 1133 temperature to increase; in fact, it may need to decrease by approximately  $0.66 \text{ K}$  to achieve the  
 1134 desired enhancement in sensible heat flux and reach equilibrium.

1135 Additionally, to assess the effectiveness of various dust scattering properties (e.g., HD27, HD09,  
 1136 and BM) in matching observations of near-surface temperature, we compare the modeled near  
 1137 surface temperature ( $T_{2m}$ ) with CRU TS observations, which is described in Section 2.6, over the  
 1138 Sahara and Sahel regions (Table 5). Considering the relatively large inter-model spread of regional  
 1139 surface air temperature, we compare the Sahara-Sahel regional contrast in surface air temperature  
 1140 to the CRU rather than comparing their absolute values. Table 5 shows that HD09 and BM improve  
 1141 the agreement with CRU in Sahara-Sahel temperature contrast compared to HD27, and BM  
 1142 exhibits the closest agreement with CRU.

1143 **Table 5.** The 19-year (2001~2019) JJA mean 2-meter Air Temperature ( $T_{2m}$ , unit: K) and their standard  
 1144 deviation over the 19 years from CRU observations and modeled experiments over the Sahara and Sahel  
 1145 regions. The ‘Contrast’ row indicates the  $T_{2m}$  regional contrast between the Sahara and the Sahel.

Region \	CRU (K)	HD27 (K)	HD09 (K)	BM (K)
Sahara	$305.8 \pm 0.18$	$306.55 \pm 0.52$	$306.2 \pm 0.68$	$305.89 \pm 0.61$
Sahel	$304.1 \pm 0.32$	$303.19 \pm 0.46$	$303.87 \pm 0.51$	$303.89 \pm 0.59$
Contrast	$1.7 \pm 0.5$	$3.36 \pm 0.98$	$2.3 \pm 1.19$	$2.0 \pm 1.2$

1146

### 1147 5.3 Impacts on winds and precipitation

1148 To understand the fast circulation and hydrological response resulting from resolving dust  
 1149 mineralogy, we examine surface wind speed anomalies (Figure 13) and precipitation anomalies

Deleted: 3

Deleted: 4

Deleted: Figure 9.

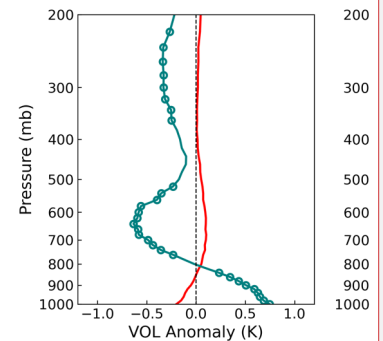
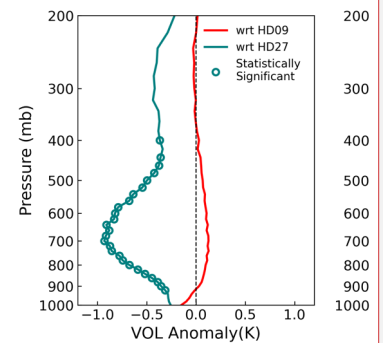
Deleted: 39

Moved up [14]: Figure 9.

Moved up [16]: Vertical profile of temperature anomaly induced by resolving dust mineralogy for the Sahara (1<sup>st</sup> row) and the Sahel (2<sup>nd</sup> row) regions in the three mineral-resolved experiments (i.e., VOL, MG, BM). Green lines represent temperature anomalies with respect to HD27

Moved up [17]: Air temperature at 2-meter from HD27 control run (a), anomaly (b) induced by implementing Bruggeman-mixing minerals in BM experiment, surface sensible heat flux (c), latent heat flux (d), net radiative flux (e), net energy flux (f) anomalies between BM and HD27;

Moved up [19]: Soil liquid content in HD27 control run (a) and anomaly resulting from implementing Bruggeman-mixing minerals in the BM experiment (b). The two values in parentheses within the title of each figure are domain average for the Sahara and Sahel regions. ¶



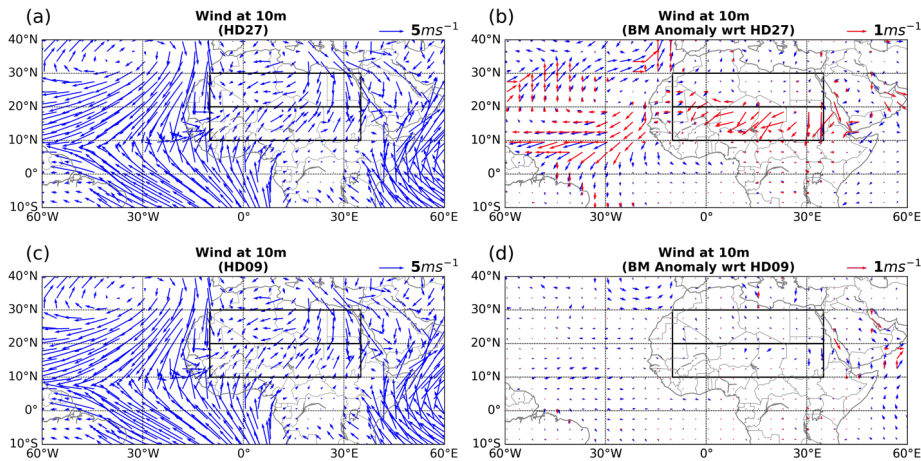
Deleted:

Deleted: 10.

Deleted: ¶

... [8]

1201 (Figure 14) induced by mineral-resolved dust. We compare mineral-resolved experiments (using  
1202 BM as an example) with HD27 and HD09, respectively, to investigate the effects of resolving dust  
1203 mineralogy.



1204  
1205 **Figure 13.** Surface wind at 10-meter from HD27 (a) and HD09 (c) control runs and their anomalies (b) and  
1206 (d) resulting from implementing Bruggeman-mixing minerals in the BM experiment. Statistically  
1207 significant wind anomalies are highlighted by red arrows.

1208 Global precipitation is higher by 0.017 mm/day for the BM mineral-speciated case compared to  
1209 HD27 experiment. This is consistent with the lower SW absorption in the former, given the global  
1210 compensation between latent heating associated with precipitation and net radiative cooling (e.g.,  
1211 Allen and Ingram, 2002; Samset, 2022). (Global radiative cooling is also compensated, although to a  
1212 smaller extent, by the sensible heat flux.)

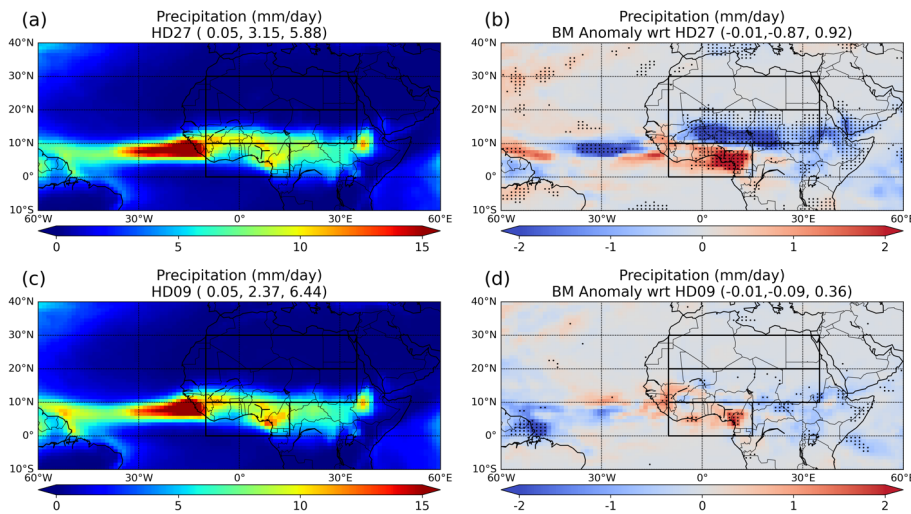
1213 However, within the Sahel, precipitation for BM is reduced compared to HD27 (Figure 14b), with  
1214 weaker onshore flow during the summer monsoon (Figure 13b), displacing West African  
1215 precipitation toward the Guinea coast. This reduction is consistent with several previous  
1216 calculations of the fast response calculated with fixed SST (e.g., Stephens et al., 2004; Miller et  
1217 al., 2004b; Lau et al., 2009; Jin et al., 2016; Jordan et al., 2018).

1218 Dust absorbs radiation and redistributes heating from the surface to within the dust layer (Miller  
1219 and Tegen, 1999; Strong et al., 2015). The heating of the air warms the lower to middle troposphere,

Moved (insertion) [20]



1220 thereby enhancing upward motion. The rising warm air spawns a large-scale onshore flow,  
 1221 carrying the low-level moist air from the Atlantic to the Sahel, thus enhancing precipitation over  
 1222 this region (Balkanski et al., 2021). The more scattering mineral-resolved BM and MG dust absorb  
 1223 less radiation and cause less warming of the atmosphere (Section 4.1), reducing adiabatic cooling  
 1224 through ascent and Sahel precipitation. The suppressed ascent in BM compared to HD27 is  
 1225 associated with a reduction both in the wind divergence aloft and in convergence at the surface  
 1226 (Figure 13b). The reduction in convergence results in northeast wind anomalies at 10-meter over  
 1227 the Sahel (Figure 13b), which are opposite in direction to the southwest onshore winds of the West  
 1228 African Monsoon (Figure 13a). The inhibition of onshore winds, bringing less moisture to the  
 1229 Sahel, is consistent with the reduction of ascent and precipitation over this region (Figure 14a, b).



1230 **Figure 14.** 19-year (2001-2019) JJA mean precipitation from HD27 (a) and HD09 (c) control runs and  
 1231 anomalies resulting from implementing Bruggeman-mixing minerals with respect to HD27 (b) and with  
 1232 respect to HD09 (d). The three values in the parenthesis are domain averaged values for the Sahara, Sahel,  
 1233 and GC regions.

1235 Besides the Sahel, there is a statistically significant positive anomaly (0.92 mm/day) of  
 1236 precipitation over the region to the south of the Sahel in BM relative to HD27 (Figure 14b). We  
 1237 will call this region the Guinea Coast (GC: 0-10°N, 10°W-15°E) region. One possible reason for  
 1238 the increase of precipitation over the GC is that the region is located to the south of the Saharan  
 1239 dust layer, where the suppression of ascent over the Sahel in BM suppresses the subsidence in the

**Moved (insertion) [21]**

**Deleted:** Figure 12) and precipitation anomalies (Figure 13) induced by mineral-resolved dust. Based on the elevated heat pump (EHP) mechanism of Lau et al., (2009), more absorptive dust absorbs radiation and redistributes heating from the surface to within the dust layer (Miller and Tegen, 1998; Strong et al., 2015). Atmospheric heating leads to ascent thus enhancing precipitation. In this sense, more scattering mineral-resolved dust aerosols absorb less radiation and cause less warming of the atmosphere, suppressing ascent motion and reducing precipitation. ¶ As discussed in the Section 4.1, mineral-resolved dust (i.e., VOL, MG, and BM) is more scattering than HD27. Relative to HD27 case, mineral-resolved dust causes less warming of the atmosphere due to less absorption and suppresses ascent. The suppressed ascent is associated with a reduction both in the wind divergence aloft and in convergence at the surface. The reduction in convergence results in northeast wind anomalies at 10-meter over the Sahel (Figure 12a, b), which are opposite in direction to the southwest onshore winds of the West African Monsoon. The inhibition of onshore winds, bringing less moisture to the Sahel, combined with the suppression of ascent motion work together to reduce precipitation over this region (Figure 13a, b). ¶

**Deleted:** 28

**Deleted:** Figure 13b), we

**Deleted:** as

1266 GC region and, therefore, enhances the precipitation (Guo et al. 2021). Alternatively, the moist  
1267 onshore flow that is weakened in BM is subject to greater dilution by the dry desert air, resulting  
1268 in reduced moist static energy and buoyancy, limiting convection to the coastal region.

1269 These changes in precipitation have non-negligible effects on soil moisture content in North Africa  
1270 due to its moisture-starved environment. The decrease in precipitation over the Sahel in BM leads  
1271 to a reduction in soil moisture content. Conversely, the increase of precipitation over the GC leads  
1272 to increases of soil moisture (Figure 12). The change in soil moisture content further affects the  
1273 partitioning of surface energy fluxes and the efficiency of the latent heat flux, thereby affecting  
1274 land surface temperature, as illustrated by Figure 11.

1275 So far, we have been focusing on discussing the impacts of resolving dust mineralogy on winds  
1276 and precipitation relative to the HD27 control run. The large discrepancy in optical properties  
1277 between HD27 and mineral-resolved dust allows us to better understand how distinct dust  
1278 absorption impacts our climate through its distinct radiative effects.

1279 As discussed in section 4.1, HD09 dust is nearly as scattering as mineral-resolved dust but exhibits  
1280 smaller regional variability. Section 5.1.2 shows that resolving dust mineralogy does not lead to  
1281 statistically significant anomalies on radiation relative to HD09. Consistently, there are no further  
1282 statistically significant impacts on winds (Figure 13c, d) and precipitation (Figure 13c, d).

1283 To investigate the effectiveness of various dust scattering properties (e.g., HD27, HD09, BM) in  
1284 matching observations of precipitation rate, we compare the modeled precipitation with CRU TS  
1285 observations over the Sahara, Sahel and GC regions (Table 6). The greater difference between  
1286 HD09, BM and CRU (i.e., HD09 – CRU and BM – CRU) indicate that more scattering HD09 and  
1287 BM lead to a larger discrepancy between the modeled precipitation and CRU observations. In  
1288 contrast, Balkanski et al. (2021) describes the same balance of increased dust absorption and Sahel  
1289 precipitation but find improved agreement with Global Precipitation Climatology Project (GPCP)  
1290 data by assuming homogeneous dust containing 3% iron oxides by volume. Contrasts between that  
1291 study and ours result from differences between the GPCP and CRU data sets, contrasts in dust  
1292 absorption (related to contrasts in the dust size distribution or assumed index of refraction), non-  
1293 dust model biases in precipitation, or differences between the slow response, computed by  
1294 Balkanski et al. (2021) and the fast response that we calculate. The fast and slow response even

Deleted: pattern

Deleted: content (Figure 11).

Field Code Changed

Deleted: aerosols with varying optical properties impact

Deleted: their

Deleted: 5.1

Deleted: Figure 12

Field Code Changed

Deleted: Furthermore, to

Deleted: This discrepancy may reflect

Deleted: model

Deleted: ,

Deleted: the absence of

Deleted: climate

Deleted: , whose inclusion can change

1308 exhibit differences in the sign of the calculated precipitation anomaly within some regions of the  
 1309 WAM (Miller and Tegen, 1998; Jordan et al., 2018).

1310 Table 6. Comparison of modeled precipitation rate (PRE, unit: mm/day) with observations from CRU TS  
 1311 dataset over 2001-2019 JJA. CRU column represents 19-year (2001-2019) JJA mean PRE over the region  
 1312 as well as 19-year standard deviation (std). HD27 – CRU column shows the 19-year mean PRE difference  
 1313 between HD27 control run and CRU observations, along with the corresponding std of this 19-year  
 1314 difference. Similar for HD09 – CRU and BM – CRU.

Comparison Region	CRU (mm/day)	HD27 – CRU (mm/day)	HD09 – CRU (mm/day)	BM – CRU (mm/day)
Sahara	0.08 ± 0.013	-0.03 ± 0.03	-0.03 ± 0.07	-0.04 ± 0.05
Sahel	2.99 ± 0.27	0.16 ± 0.56	-0.62 ± 0.43	-0.71 ± 0.41
Guinea Coast	6.16 ± 0.49	-0.28 ± 0.90	0.28 ± 1.02	0.64 ± 0.83

1315

## 1316 6 Potential for reducing mineral tracers

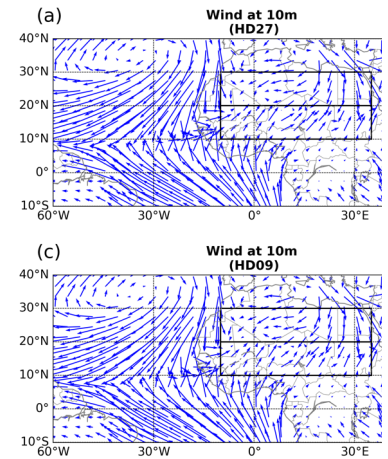
1317 Thus far in this study, we have been using 45 mineral tracers in mineral-resolved experiments (i.e.,  
 1318 VOL, MG, and BM). However, it is important to investigate the potential of reducing the number  
 1319 of mineral tracers in climate models to lower computational costs. In this section, we take BM as  
 1320 a reference for providing the best comparisons with CRU temperature and CERES flux  
 1321 observations, and conduct an experiment named BM-RT to assess the possibility of reducing  
 1322 mineral tracers in BM. The BM-RT experiment consists of three sub-experiments, namely, BM-  
 1323 LC, BM-LCRH, and BM-LCRHRG. In each of the three sub-experiments, the number of mineral  
 1324 tracers is progressively reduced, allowing for an examination of the relative impacts of different  
 1325 minerals on climate compared to the reference BM.

1326 As discussed in section 4.1, the three clay minerals (i.e., illite, kaolinite, smectite) exhibit similar  
 1327 optical properties and perform similar functions in climate by hosting hematite. Hence, they can  
 1328 be combined in their interaction with radiation without significant impacts on climate. In addition,  
 1329 by lumping the three clay minerals together, the number of mineral tracers can be reduced from  
 1330 45 in BM (nine types of minerals × five size bins) to 35 (seven types of minerals × five size bins).

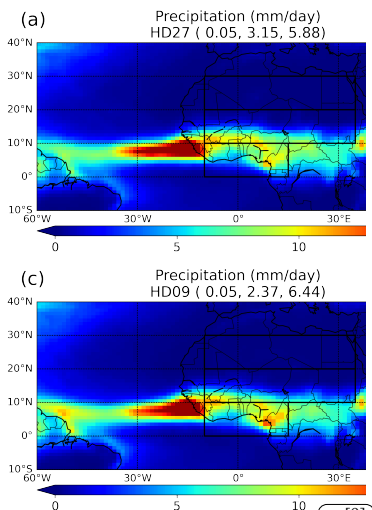
Moved up [18]: Figure 12.

Moved up [20]: Surface wind at 10-meter from HD27 (a) and HD09 (c) control runs and their anomalies (b) and (d) resulting from implementing Bruggeman-mixing minerals in the BM experiment. Statistically significant wind anomalies are highlighted by red arrows.

Moved up [21]: 19-year (2001-2019) JJA mean precipitation from HD27 (a) and HD09 (c) control runs and anomalies resulting from implementing Bruggeman-mixing minerals with respect to HD27 (b) and with respect to HD09 (d). The three values in the parenthesis are domain averaged values for the Sahara, Sahel, and GC regions.



Deleted:



Deleted:

Deleted: Note, for anomalies, we only average the dotted area, in other words, we only calculate the domain average of statistically significant anomalies.

1350 Therefore, in the first sub-experiment BM-LC (where ‘LC’ represents ‘Lump Clay minerals’), we  
1351 lump together the three clay minerals as one mineral species ‘clay433’.

1352 ~~Based upon the C1999 soil mineral composition that we use, externally~~ mixed hematite is mainly  
1353 concentrated over the Sahel region (Ginoux et al. 2023, in preparation) and cannot be transported  
1354 to remote regions due to its high ~~mass~~ density. Obiso et al. (2023) shows that ~~visible~~ extinction  
1355 due to ~~externally mixed~~ hematite is negligible compared to ~~other mineral components including~~  
1356 ~~hematite~~ internally mixed ~~with~~ other minerals. Thus, we further remove external hematite tracers  
1357 in the second sub-experiment BM-LCRH (where ‘RH’ indicates ‘Remove externally mixed  
1358 Hematite’). The mass fraction of external hematite is combined with internal hematite to ensure  
1359 that the total mineral fraction at emission remains equal to one. In this sub-experiment, the number  
1360 of mineral tracers is reduced from 35 in BM-LC to 30 in BM-LCRH.

1361 Since there are no known specific impacts of gypsum on climate, we conducted the third sub-  
1362 experiment, BM-LCRHRG (‘RG’ indicates ‘Remove Gypsum’), where gypsum was removed. The  
1363 mass fraction previously attributed to gypsum at emission, which is very low at the global scale,  
1364 was proportionally redistributed among all other minerals. The number of mineral tracers is finally  
1365 reduced from 30 in BM-LCRH to 25 in BM-LCRHRG.

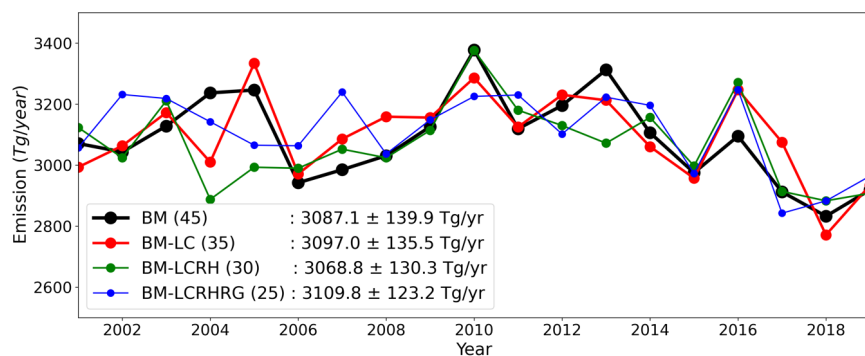
1366 We analyze the 19-year (2001-2019) time series of total dust mineral emission before and after  
1367 reducing mineral tracers in Figure 15. We observe subtle differences in total mineral emission  
1368 between experiments, which arises from the feedback of mineral radiative interactions. However,  
1369 these differences are numerically small, and Student’s t-test suggests that the time series of the  
1370 four experiments are not statistically different. Additionally, the globally averaged DAOD and  
1371 SSA of each sub-experiment remains highly similar to those of the reference experiment BM, as  
1372 listed in Table 3.

Deleted: Externally

Deleted: external

Deleted: hematite and

Field Code Changed



1376

1377 Figure 15. Time series of total dust mineral emission from 2001 to 2019 before and after reducing the  
 1378 number of mineral tracers. The legend displays the following information: ‘Experiment name (number of  
 1379 mineral tracers): 19-year averaged total mineral emission ± 19-year standard deviation of total mineral  
 1380 emission’.

1381 Given the highly similar optical properties of minerals before and after reducing mineral tracers,  
 1382 we further investigate their impact on climate. Firstly, we examine the clear-sky flux anomaly of  
 1383 each of the three sub-experiments at TOA and surface relative to the reference experiment BM, as  
 1384 shown in Supplementary Figure S14 for TOA and Supplementary Figure S15 for surface. We only  
 1385 observe a few statistically significant (p-value < 0.05) anomalies over the North Africa, suggesting  
 1386 that the reduction of mineral tracers in the three sub-experiments has a weak impact on radiation.

Deleted: S12

Deleted: S13

1387 Furthermore, we investigate the anomaly in temperature profile, surface winds, and precipitation  
 1388 of each of the three sub-experiments relative to the reference experiment BM. The results are  
 1389 presented in Figure S16-S18 in the Supplement. No statistically significant (p-value < 0.05)  
 1390 temperature anomalies (Figure S16) and surface wind anomalies (Figure S17) is observed. Only a  
 1391 few statistically significant anomalies in precipitation are observed in the Supplementary Figure  
 1392 S18. These results suggest that the reduction of mineral tracers in the three sub-experiments has a  
 1393 weak impact on climate.

Deleted: S14-

Deleted: S14

Deleted: S15

Deleted: S16

1394 The results from the BM-RT experiment suggest combining clay minerals and excluding the  
 1395 externally mixed hematite and gypsum to simulate dust impact on radiation. This does not preclude  
 1396 similar conclusion for other impacts of dust on the Earth’s climate systems. The removal of mineral  
 1397 tracers reduces the number of mineral tracers from 45 to 25, effectively lowering computational  
 1398 costs without causing statistically significant impacts on simulating climate.

Deleted: in the dust mineral implementation.

1406 **7 Conclusions**

1407 We simulate the distribution of dust mineralogy (i.e., illite, kaolinite, smectite, hematite, calcite,  
1408 feldspar, quartz, and gypsum) and activate their interaction with radiation in the GFDL AM4.0  
1409 model. Our investigation focuses on the radiative impacts of resolving dust mineralogy on Earth's  
1410 atmosphere and its fast response of land temperature, surface winds and precipitation.

1411 We set up two baseline homogeneous dust control runs: HD27 and HD09, in which dust  
1412 mineralogy is considered as temporally and spatially uniform, the former following the standard  
1413 configuration for the dust optical properties in GFDL AM4.0 and the latter including a more  
1414 scattering dust. Three experiments with resolved mineralogy are also conducted: VOL, MG, and  
1415 BG, using three different mixing rules for the internal mixture between hematite and clay minerals  
1416 (i.e., volume weighted mean, Maxwell Garnett, and Bruggeman). The comparison of dust  
1417 absorption properties (e.g., SSA) with observation-based results suggests that the homogeneous  
1418 dust used in the standard GFDL AM4.0 (i.e., HD27) is overly absorptive, Maxwell Garnett and  
1419 Bruggeman mixing rules are more appropriate than volume weighted mixing rule in calculating  
1420 optical properties of internal mixtures of hematite and clays. Compared to HD27, the homogeneous  
1421 dust with reduced hematite content (HD09) and mineral-resolved dust (i.e., MG and BM) exhibit  
1422 much better agreement with AERONET retrievals and laboratory measurements in terms of dust  
1423 absorption properties (i.e., SSA). Additionally, resolving dust mineralogy enhances regional  
1424 variability in dust SSA compared to homogenous dust, further improves the agreement with  
1425 AERONET, even though it remains lower than the observed variability.

1426 The two homogeneous dust control runs, HD27 and HD09, with distinct dust absorption properties,  
1427 allow us to investigate the impact of dust mineralogy on Earth's radiation and fast climate response  
1428 relative to distinct baseline homogeneous dust. In comparison to HD27, resolving mineralogy  
1429 reduces dust absorption. During JJA, the reduced dust absorption results in a reduction of over 50%  
1430 in NET downward radiation across the Sahara and approximately 20% over the Sahel at TOA.  
1431 Additionally, there is a reduction of around 25% in the atmospheric absorption of radiation over  
1432 the Shahara and around 10% over the Sahel in the atmosphere. The reduced surface absorption of  
1433 radiation by mineral-resolved dust leads to a temperature decrease of 0.66 K at the land surface  
1434 across the Sahara and an increase of 0.7 K over the Sahel. The reduced NET downward radiation  
1435 at TOA, attributed to the less absorption of radiation by mineral-resolved dust, suppresses ascent

Deleted: .

Deleted: mineral-resolved

Deleted: . During JJA, compared

Deleted: dust

Deleted: 39K

Deleted: 6K

1442 and weakens the monsoon inflow from the Gulf of Guinea. This brings less moisture to the Sahel,  
1443 which combined with decreased ascent induces a reduction of precipitation. On the other hand,  
1444 compared to HD09, resolving dust mineralogy results in dust absorption comparable to that of  
1445 HD09 on a global scale. However, when resolving mineralogy, there is an increase in spatial  
1446 variation of dust absorption. Additionally, we observe a noticeable change in global distribution  
1447 of dust absorption, with more dust absorption distributed in the Southern Hemisphere and lower  
1448 dust absorption over Iceland and Taklamakan regions. Nevertheless, the higher spatial variation in  
1449 dust absorption does not lead to statistically significant changes in any of the climate aspects  
1450 mentioned above. The models with reduced absorption (HD09 and fully resolved mineralogy)  
1451 improve the comparison with observations of CERES fluxes and CRU land surface temperature.  
1452 We see a slightly better agreement with observations for fully resolved mineralogy than HD09  
1453 however it is not statistically significant. As such, when using fixed mineralogical composition,  
1454 we recommend using a 0.9% hematite content in volume, which represents the lowest of the three  
1455 hematite mixings considered by Balkanski et al. (2007).

1456 Historically, climate models have relied on fixed refractive index to consider dust radiative forcing  
1457 starting (IPCC, 2001) with strongly absorptive value based on dust samples in Sahara (Patterson  
1458 et al., 1977) to more scattering values after dust absorption could be inferred from satellite and  
1459 surface observations (e.g., Sinyuk et al., 2003; Balkanski et al., 2007). With the launch of EMIT  
1460 in July 2022 and the expected delivery of a high-resolution map of soil mineralogy in source areas,  
1461 dust interactions with radiation in climate models will be calculated directly from the simulated  
1462 mineralogical composition (Li et al., 2021). Still, the additional burden of simulating a dozen  
1463 minerals may be too prohibitive for large ensemble climate models simulations. In such cases, our  
1464 analysis suggests the use of a fixed value providing similar radiative effects as the comprehensive  
1465 representation of minerals. However, our recommendation is directed toward the GFDL AM4.0  
1466 model with all its uncertainties related to mineral distribution, emission sources, and aerosol  
1467 transport. Moreover, incorporating dust mineralogy in models is likely to be important, in other  
1468 aspects, such as cloud properties, ocean biogeochemistry, air quality and photochemistry. For  
1469 studies with resolved mineralogy, we show that the number of mineral tracers can be reduced from  
1470 45 to 25 without losing the quality of comparison with observations of CERES fluxes and CRU  
1471 surface temperature. Such reduction can be achieved by lumping together clay minerals, removing

Deleted: all above-

Deleted: aspects compared to HD09

Deleted: also

1475 external hematite and gypsum. For specific research such as biogeochemistry, it may be necessary  
1476 to fully resolve mineralogy to achieve accuracy.

1477 This study has some limitations. First, the soil mineralogy map from C1999 is based on extensive  
1478 extrapolation and limited observations. In terms of the need to improve knowledge of soil  
1479 mineralogy in dust source regions, the launch in July 2022 of the EMIT instrument operating from  
1480 the International Space Station will provide mineral identifications of dust sources using  
1481 hyperspectral measurements (Green et al., 2020). The EMIT soil map measurements will improve  
1482 resolving dust mineralogy in climate models and advance our understanding of dust's effects in  
1483 the Earth system. Second, hematite and goethite are the most common iron oxides present in soils.  
1484 However, goethite is not considered in this study because not included in the used soil mineralogy  
1485 map. Previous studies suggest that goethite is generally more abundant than hematite, but it is less  
1486 absorptive than hematite in the visible spectrum (Formenti et al., 2014). Therefore, the abundance  
1487 of iron oxides may be underestimated in this study, which may lead to underestimation of dust  
1488 absorption in the SW. A more recent database by Journet et al. (2014) (J2014) includes the  
1489 distribution of goethite but it shares many limitations as C1999 (e.g., extensive extrapolation) and  
1490 has other major disadvantages, such as numbers of missing soil fractions of some minerals at some  
1491 locations. Third, the refractive index of hematite used in our study is close to the upper range of  
1492 the values available in literature (Zhang et al., 2015). Hence, the last two limitations,  
1493 underestimation of iron oxide content and overestimation of absorption by hematite, may have  
1494 compensating effects.

1495 This study, by prescribing SST, calculates only the fast response to the dust DRE, without  
1496 including the slow response by the sea surface temperature. This avoids the need to spin-up the  
1497 model for decades before reaching new equilibrium but may overestimate the eventual response,  
1498 as shown by Miller and Tegen (1998) and Balkanski et al. (2021). This complicates model  
1499 evaluation because the observations include the slow response to dust. Variables like precipitation  
1500 are especially sensitive to the inclusion of the slow response because prescribed SST experiments  
1501 omit the surface energy balance over the ocean. Thus, the surface DRE beneath the aerosol layer,  
1502 which is generally negative, is not fully balanced by a fast reduction of evaporation (Miller et al.,  
1503 2004a). The addition of the surface balance in the slow response can reverse the sign of the fast  
1504 precipitation anomaly (Miller and Tegen, 1998; Jordan et al., 2018). In this study, the increase of  
1505 dust scattering (e.g., through consideration of dust mineral composition) generally reduces model

Deleted: .

Deleted: (Miller et al., 2004)



1508 biases for all variables except precipitation. Future works may include satellite-based inventory of  
1509 soil mineralogy using fully coupled Earth's system components.

1510 **8 Competing interests**

1511 The contact author has declared that none of the authors has any competing interests.

1512 **9 Acknowledgement**

1513 This research is supported by a collaboration between Princeton University and NOAA GFDL,  
1514 Cooperative Institute for Modeling the Earth System (CIMES). A portion of this work is funded  
1515 by the Earth Surface Mineral Dust Source Investigation (EMIT), a NASA Earth Ventures-  
1516 Instrument (EVI-4) Mission. Carlos Pérez García-Pando and María Gonçalves Ageitos  
1517 acknowledge support from the European Research Council (ERC) under the Horizon 2020  
1518 research and innovation program through the ERC Consolidator Grant FRAGMENT (grant  
1519 agreement no. 773051), the AXA Research Fund through the AXA Chair on Sand and Dust Storms  
1520 at the Barcelona Supercomputing Center (BSC), the European Union's Horizon 2020 research and  
1521 innovation program under grant agreement no. 821205 (FORCeS) and the Department of Research  
1522 and Universities of the Government of Catalonia via the Research Group Atmospheric  
1523 Composition (code 2021 SGR 01550). Vincenzo Obiso was supported by the NASA Postdoctoral  
1524 Program at the NASA Goddard Institute for Space Studies administered by Oak Ridge Associated  
1525 Universities under contract with NASA (80HQTR21CA005). We acknowledge the CERES EBAF  
1526 Ed 4.2 data, which were obtained from the NASA Langley Research Center CERES ordering tool  
1527 at <https://ceres.larc.nasa.gov/data/>.

1528

1529 **10 References**

- 1530 [Allen, M. R. and Ingram, W. J.: Constrains on future changes in climate and the hydrologic cycle,](#)  
1531 [419, 224–232, 2002.](#)
- 1532 Atkinson, J. D., Murray, B. J., Woodhouse, M. T., Whale, T. F., Baustian, K. J., Carslaw, K. S.,  
1533 Dobbie, S., O’Sullivan, D., and Malkin, T. L.: The importance of feldspar for ice nucleation by  
1534 mineral dust in mixed-phase clouds, *Nature*, 498, 355–358, <https://doi.org/10.1038/nature12278>,  
1535 2013.
- 1536 Balkanski, Y., Schulz, M., Claquin, T., and Guibert, S.: Reevaluation of Mineral aerosol radiative  
1537 forcings suggests a better agreement with satellite and AERONET data, *Atmos. Chem. Phys.*, 7,  
1538 81–95, <https://doi.org/DOI.10.5194/acp-7-81-2007>, 2007.
- 1539 [Balkanski, Y., Bonnet, R., Boucher, O., Checa-Garcia, R., and Servonnat, J.: Better representation](#)  
1540 [of dust can improve climate models with too weak an African monsoon, \*Atmos. Chem. Phys.\*, 21,](#)  
1541 [11423–11435, <https://doi.org/10.5194/acp-21-11423-2021>, 2021.](#)
- 1542 Di Biagio, C., Formenti, P., Balkanski, Y., Caponi, L., Cazaunau, M., Pangui, E., Journet, E.,  
1543 Nowak, S., Caquineau, S., Andreae O, M., Kandler, K., Saeed, T., Piketh, S., Seibert, D., Williams,  
1544 E., and Doussin, J. F. C.: Global scale variability of the mineral dust long-wave refractive index:  
1545 A new dataset of in situ measurements for climate modeling and remote sensing, *Atmos. Chem.*  
1546 *Phys.*, 17, 1901–1929, <https://doi.org/10.5194/acp-17-1901-2017>, 2017.
- 1547 Di Biagio, C., Formenti, P., Balkanski, Y., Caponi, L., Cazaunau, M., Pangui, E., Journet, E.,  
1548 Nowak, S., Andreae, M. O., Kandler, K., Saeed, T., Piketh, S., Seibert, D., Williams, E., and  
1549 Doussin, J. F.: Complex refractive indices and single-scattering albedo of global dust aerosols in  
1550 the shortwave spectrum and relationship to size and iron content, *Atmos. Chem. Phys.*, 19, 15503–  
1551 15531, <https://doi.org/10.5194/acp-19-15503-2019>, 2019.
- 1552 Bian, H. and Zender, C. S.: Mineral dust and global tropospheric chemistry: Relative roles of  
1553 photolysis and heterogeneous uptake, *J. Geophys. Res. Atmos.*, 108,  
1554 <https://doi.org/10.1029/2002jd003143>, 2003.
- 1555 Bullard, J. E., Harrison, S. P., Baddock, M. C., Drake, N., Gill, T. E., McTainsh, G., and Sun, Y.:  
1556 Preferential dust sources: A geomorphological classification designed for use in global dust-cycle

1557 models, *J. Geophys. Res. Earth Surf.*, 116, <https://doi.org/10.1029/2011JF002061>, 2011.

1558 Chatziparaschos, M., Daskalakis, N., Myriokefalitakis, S., Kalivitis, N., Nenes, A., Goncalves  
1559 Ageitos, M., Costa-Suares, M., Perez Garcia-Pando, C., Zanolli, M., Vrekoussis, M., and Kanakidou,  
1560 M.: Role of K-feldspar and quartz in global ice nucleation by mineral dust in mixed-phase clouds,  
1561 *Atmos. Chem. Phys.*, 23, 1785–1801, <https://doi.org/10.5194/acp-23-1785-2023>, 2023.

1562 Claquin, T., SCHULZ, M., BALKANSKI, Y., and BOUCHER, O.: Uncertainties in assessing  
1563 radiative forcing by mineral dust, *Tellus B*, 50, 491–505, <https://doi.org/10.1034/j.1600->  
1564 0889.1998.t01-2-00007.x, 1998.

1565 Claquin, T., Schulz, M., and Balkanski, Y. J.: Modeling the mineralogy of atmospheric dust  
1566 sources, *J. Geophys. Res. Atmos.*, 104, 22243–22256, <https://doi.org/10.1029/1999JD900416>,  
1567 1999.

1568 [Delworth, T. L., Broccoli, A. J., Rosati, A., Stouffer, R. J., Balaji, V., Beesley, J. A., Cooke, W.](#)  
1569 [F., Dixon, K. W., Dunne, J., Dunne, K. A., Durachta, J. W., Findell, K. L., Ginoux, P.,](#)  
1570 [Gnanadesikan, A., Gordon, C. T., Griffies, S. M., Gudgel, R., Harrison, M. J., Held, I. M., Hemler,](#)  
1571 [R. S., Horowitz, L. W., Klein, S. A., Knutson, T. R., Kushner, P. J., Langenhorst, A. R., Lee, H.](#)  
1572 [C., Lin, S. J., Lu, J., Malyshev, S. L., Milly, P. C. D., Ramaswamy, V., Russell, J., Schwarzkopf,](#)  
1573 [M. D., Shevliakova, E., Sirutis, J. J., Spelman, M. J., Stern, W. F., Winton, M., Wittenberg, A. T.,](#)  
1574 [Wyman, B., Zeng, F., and Zhang, R.: GFDL's CM2 global coupled climate models. Part I:](#)  
1575 [Formulation and simulation characteristics, \*J. Clim.\*, 19, 643–674,](#)  
1576 <https://doi.org/10.1175/JCLI3629.1>, 2006.

1577 Dentener, F. J., Carmichael, G. R., Zhang, Y., Lelieveld, J., and Crutzen, P. J.: Role of mineral  
1578 aerosol as a reactive surface in the global troposphere, *J. Geophys. Res. Atmos.*, 101, 22869–22889,  
1579 <https://doi.org/10.1029/96jd01818>, 1996.

1580 [Donner, L. J., Wyman, B. L., Hemler, R. S., Horowitz, L. W., Ming, Y., Zhao, M., Golaz, J. C.,](#)  
1581 [Ginoux, P., Lin, S. J., Schwarzkopf, M. D., Austin, J., Alaka, G., Cooke, W. F., Delworth, T. L.,](#)  
1582 [Freidenreich, S. M., Gordon, C. T., Griffies, S. M., Held, I. M., Hurlin, W. J., Klein, S. A., Knutson,](#)  
1583 [T. R., Langenhorst, A. R., Lee, H. C., Lin, Y., Magi, B. I., Malyshev, S. L., Milly, P. C. D., Naik,](#)  
1584 [V., Nath, M. J., Pincus, R., Ploshay, J. J., Ramaswamy, V., Seman, C. J., Shevliakova, E., Sirutis,](#)  
1585 [J. J., Stern, W. F., Stouffer, R. J., Wilson, R. J., Winton, M., Wittenberg, A. T., and Zeng, F.: The](#)

1586 [dynamical core, physical parameterizations, and basic simulation characteristics of the](#)  
1587 [atmospheric component AM3 of the GFDL global coupled model CM3, \*J. Clim.\*, 24, 3484–3519,](#)  
1588 <https://doi.org/10.1175/2011JCLI3955.1>, 2011.

1589 Dubovik, O., Holben, B., Eck, T. F., Smirnov, A., Kaufman, Y. J., King, M. D., Tanre, D., and  
1590 Slutsker, I.: Variability of absorption and optical properties of key aerosol types observed in  
1591 worldwide locations, *J. Atmos. Sci.*, 59, 590–608, [https://doi.org/Doi%2010.1175/1520-](https://doi.org/Doi%2010.1175/1520-0469(2002)059<0590:Voaap>2.0.Co;2)  
1592 [0469\(2002\)059<0590:Voaap>2.0.Co;2](https://doi.org/Doi%2010.1175/1520-0469(2002)059<0590:Voaap>2.0.Co;2), 2002.

1593 Dunne, J. P., Horowitz, L. W., Adcroft, A. J., Ginoux, P., Held, I. M., John, J. G., Krasting, J. P.,  
1594 Malyshev, S., Naik, V., Paulot, F., Shevliakova, E., Stock, C. A., Zadeh, N., Balaji, V., Blanton,  
1595 C., Dunne, K. A., Dupuis, C., Durachta, J., Dussin, R., Gauthier, P. P. G., Griffies, S. M., Guo, H.,  
1596 Hallberg, R. W., Harrison, M., He, J., Hurlin, W., McHugh, C., Menzel, R., Milly, P. C. D.,  
1597 Nikonov, S., Paynter, D. J., Ploshay, J., Radhakrishnan, A., Rand, K., Reichl, B. G., Robinson, T.,  
1598 Schwarzkopf, D. M., Sentman, L. T., Underwood, S., Vahlenkamp, H., Winton, M., Wittenberg,  
1599 A. T., Wyman, B., Zeng, Y., and Zhao, M.: The GFDL Earth System Model Version 4.1 (GFDL-  
1600 ESM 4.1): Overall Coupled Model Description and Simulation Characteristics, *J. Adv. Model.*  
1601 *Earth Syst.*, 12, <https://doi.org/10.1029/2019MS002015>, 2020.

1602 Evans, S., Malyshev, S., Ginoux, P., and Shevliakova, E.: The Impacts of the Dust Radiative Effect  
1603 on Vegetation Growth in the Sahel, *Global Biogeochem. Cycles*, 33, 1582–1593,  
1604 <https://doi.org/10.1029/2018GB006128>, 2019.

1605 Formenti, P., Caquineau, S., Chevaillier, S., Klaver, A., Desboeufs, K., Rajot, J. L., Belin, S., and  
1606 Briois, V.: Dominance of goethite over hematite in iron oxides of mineral dust from Western  
1607 Africa: Quantitative partitioning by X-ray absorption spectroscopy, *J. Geophys. Res. Atmos.*, 119,  
1608 12,740–12,754, <https://doi.org/10.1002/2014JD021668>, 2014.

1609 Gates, W. L.: AMIP: the Atmospheric Model Intercomparison Project, *Bull. - Am. Meteorol. Soc.*,  
1610 73, 1962–1970, [https://doi.org/10.1175/1520-0477\(1992\)073<1962:ATAMIP>2.0.CO;2](https://doi.org/10.1175/1520-0477(1992)073<1962:ATAMIP>2.0.CO;2), 1992.

1611 Giles, D. M., Sinyuk, A., Sorokin, M. G., Schafer, J. S., Smirnov, A., Slutsker, I., Eck, T. F.,  
1612 Holben, B. N., Lewis, J. R., Campbell, J. R., Welton, E. J., Korkin, S. V., and Lyapustin, A. I.:  
1613 Advancements in the Aerosol Robotic Network (AERONET) Version 3 database - Automated  
1614 near-real-time quality control algorithm with improved cloud screening for Sun photometer

1615 aerosol optical depth (AOD) measurements, *Atmos. Meas. Tech.*, 12, 169–209,  
1616 <https://doi.org/10.5194/amt-12-169-2019>, 2019.

1617 Ginoux, P.: Effects of nonsphericity on mineral dust modeling, *J. Geophys. Res. Atmos.*, 108,  
1618 <https://doi.org/10.1029/2002jd002516>, 2003.

1619 Ginoux, P., Chin, M., Tegen, I., Prospero, J. M., Holben, B., Dubovik, O., and Lin, S. J.: Sources  
1620 and distributions of dust aerosols simulated with the GOCART model, *J. Geophys. Res.*, 106,  
1621 20255–20273, <https://doi.org/10.1029/2000jd000053>, 2001.

1622 Gliß, J., Mortier, A., Schulz, M., Andrews, E., Balkanski, Y., Bauer, S. E., Benedictow, A. M. K.,  
1623 Bian, H., Checa-Garcia, R., Chin, M., Ginoux, P., Griesfeller, J. J., Heckel, A., Kipling, Z.,  
1624 Kirkevåg, A., Kokkola, H., Laj, P., Le Sager, P., Tronstad Lund, M., Lund Myhre, C., Matsui, H.,  
1625 Myhre, G., Neubauer, D., Van Noije, T., North, P., Olivié, D. J. L., Rémy, S., Sogacheva, L.,  
1626 Takemura, T., Tsigaridis, K., and Tsyro, S. G.: AeroCom phase III multi-model evaluation of the  
1627 aerosol life cycle and optical properties using ground- And space-based remote sensing as well as  
1628 surface in situ observations, *Atmos. Chem. Phys.*, 21, 87–128, [https://doi.org/10.5194/acp-21-87-](https://doi.org/10.5194/acp-21-87-2021)  
1629 2021, 2021.

1630 Gonçalves Ageitos, M., Obiso, V., Miller, R. L., Jorba, O., Klose, M., Dawson, M., Balkanski, Y.,  
1631 Perlwitz, J., Basart, S., Di Tomaso, E., Escribano, J., MacChia, F., Montané, G., Mahowald, N.  
1632 M., Green, R. O., Thompson, D. R., and Pérez García-Pando, C.: Modeling dust mineralogical  
1633 composition: sensitivity to soil mineralogy atlases and their expected climate impacts, *Atmos.*  
1634 *Chem. Phys.*, 23, 8623–8657, <https://doi.org/10.5194/acp-23-8623-2023>, 2023.

1635 Green, R. O., Mahowald, N., Ung, C., Thompson, D. R., Bator, L., Bennet, M., Bernas, M.,  
1636 Blackway, N., Bradley, C., Cha, J., Clark, P., Clark, R., Cloud, D., Diaz, E., Ben Dor, E., Duren,  
1637 R., Eastwood, M., Ehlmann, B. L., Fuentes, L., Ginoux, P., Gross, J., He, Y., Kalashnikova, O.,  
1638 Kert, W., Keymeulen, D., Klimesh, M., Ku, D., Kwong-Fu, H., Liggett, E., Li, L., Lundeen, S.,  
1639 Makowski, M. D., Mazer, A., Miller, R., Mouroulis, P., Oaida, B., Okin, G. S., Ortega, A., Oyake,  
1640 A., Nguyen, H., Pace, T., Painter, T. H., Pempejian, J., Garcia-Pando, C. P., Pham, T., Phillips, B.,  
1641 Pollock, R., Purcell, R., Realmuto, V., Schoolcraft, J., Sen, A., Shin, S., Shaw, L., Soriano, M.,  
1642 Swayze, G., Thingvold, E., Vaid, A., and Zan, J.: The Earth Surface Mineral Dust Source  
1643 Investigation: An Earth Science Imaging Spectroscopy Mission, in: 2020 IEEE Aerospace  
1644 Conference, 1–15, <https://doi.org/10.1109/AERO47225.2020.9172731>, 2020.

1645 Grider, A., Ponette-González, A., and Heindel, R.: Calcium and ammonium now control the pH  
1646 of wet and bulk deposition in Ohio, U.S., *Atmos. Environ.*, 310,  
1647 <https://doi.org/10.1016/j.atmosenv.2023.119986>, 2023.

1648 Guo, H., Ming, Y., Fan, S., Zhou, L., Harris, L., and Zhao, M.: Two-Moment Bulk Cloud  
1649 Microphysics With Prognostic Precipitation in GFDL's Atmosphere Model AM4.0: Configuration  
1650 and Performance, *J. Adv. Model. Earth Syst.*, 13, <https://doi.org/10.1029/2020MS002453>, 2021.

1651 Harris, I., Osborn, T. J., Jones, P., and Lister, D.: Version 4 of the CRU TS monthly high-resolution  
1652 gridded multivariate climate dataset, *Sci. Data*, 7, <https://doi.org/10.1038/s41597-020-0453-3>,  
1653 2020.

1654 Harrison, A. D., Lever, K., Sanchez-Marroquin, A., Holden, M. A., Whale, T. F., Tarn, M. D.,  
1655 McQuaid, J. B., and Murray, B. J.: The ice-nucleating ability of quartz immersed in water and its  
1656 atmospheric importance compared to K-feldspar, *Atmos. Chem. Phys.*, 19, 11343–11361,  
1657 <https://doi.org/10.5194/acp-19-11343-2019>, 2019.

1658 Huang, Y., Kok, J. F., Saito, M., and Muñoz, O.: Single-scattering properties of ellipsoidal dust  
1659 aerosols constrained by measured dust shape distributions, *Atmos. Chem. Phys.*, 23, 2557–2577,  
1660 <https://doi.org/10.5194/acp-23-2557-2023>, 2023.

1661 Huneus, N., Schulz, M., Balkanski, Y., Griesfeller, J., Prospero, J., Kinne, S., Bauer, S., Boucher,  
1662 O., Chin, M., Dentener, F., Diehl, T., Easter, R., Fillmore, D., Ghan, S., Ginoux, P., Grini, A.,  
1663 Horowitz, L., Koch, D., Krol, M. C., Landing, W., Liu, X., Mahowald, N., Miller, R., Morcrette,  
1664 J. J., Myhre, G., Penner, J., Perlwitz, J., Stier, P., Takemura, T., and Zender, C. S.: Global dust  
1665 model intercomparison in AeroCom phase i, *Atmos. Chem. Phys.*, 11, 7781–7816,  
1666 <https://doi.org/10.5194/acp-11-7781-2011>, 2011.

1667 [Jin, Q., Yang, Z. L., and Wei, J.: High sensitivity of Indian summer monsoon to Middle East dust](#)  
1668 [absorptive properties, \*Sci. Rep.\*, 6, <https://doi.org/10.1038/srep30690>, 2016.](#)

1669 Jordan, A. K., Gnanadesikan, A., and Zaitchik, B.: Simulated dust aerosol impacts on western  
1670 sahelian rainfall: Importance of ocean coupling, *J. Clim.*, 31, 9107–9124,  
1671 <https://doi.org/10.1175/JCLI-D-17-0819.1>, 2018.

1672 Journet, E., Balkanski, Y., and Harrison, S. P.: A new data set of soil mineralogy for dust-cycle  
1673 modeling, *Atmos. Chem. Phys.*, 14, 3801–3816, <https://doi.org/10.5194/acp-14-3801-2014>, 2014.

1674 [Kandler, K., Schutz, L., Deutscher, C., Ebert, M., Hofmann, H., Jackel, S., Jaenicke, R., Knippertz,](#)  
1675 [P., Lieke, K., Massling, A., Petzold, A., Schladitz, A., Weinzierl, B., Wiedensohler, A., Zorn, S.,](#)  
1676 [and Weinbruch, S.: Size distribution, mass concentration, chemical and mineralogical composition](#)  
1677 [and derived optical parameters of the boundary layer aerosol at Tinfou, Morocco, during SAMUM](#)  
1678 [2006, \*Tellus Ser. B-Chemical Phys. Meteorol.\*, 61, 32–50, \[https://doi.org/10.1111/j.1600-\]\(https://doi.org/10.1111/j.1600-0889.2008.00385.x\)](#)  
1679 [0889.2008.00385.x, 2009.](#)

1680 Kelly, J. T., Chuang, C. C., and Wexler, A. S.: Influence of dust composition on cloud droplet  
1681 formation, *Atmos. Environ.*, 41, 2904–2916, <https://doi.org/10.1016/j.atmosenv.2006.12.008>,  
1682 2007.

1683 Kok, J. F.: A scaling theory for the size distribution of emitted dust aerosols suggests climate  
1684 models underestimate the size of the global dust cycle, *Proc. Natl. Acad. Sci. U. S. A.*, 108, 1016–  
1685 1021, <https://doi.org/10.1073/pnas.1014798108>, 2011.

1686 Kok, J. F., Ridley, D. A., Zhou, Q., Miller, R. L., Zhao, C., Heald, C. L., Ward, D. S., Albani, S.,  
1687 and Haustein, K.: Smaller desert dust cooling effect estimated from analysis of dust size and  
1688 abundance, *Nat. Geosci.*, 10, 274–278, <https://doi.org/10.1038/Ngeo2912>, 2017.

1689 [Kok, J. F., Adebisi, A. A., Albani, S., Balkanski, Y., Checa-Garcia, R., Chin, M., Colarco, P. R.,](#)  
1690 [Hamilton, D. S., Huang, Y., Ito, A., Klose, M., Leung, D. M., Li, L., Mahowald, N. M., Miller, R.](#)  
1691 [L., Obiso, V., Pérez García-Pando, C., Rocha-Lima, A., Wan, J. S., and Whicker, C. A.: Improved](#)  
1692 [representation of the global dust cycle using observational constraints on dust properties and](#)  
1693 [abundance, \*Atmos. Chem. Phys.\*, 21, 8127–8167, <https://doi.org/10.5194/acp-21-8127-2021>, 2021.](#)

1694 Lau, K. M., Kim, K. M., Sud, Y. C., and Walker, G. K.: A GCM study of the response of the  
1695 atmospheric water cycle of West Africa and the Atlantic to Saharan dust radiative forcing, *Ann.*  
1696 *Geophys.*, 27, 4023–4037, <https://doi.org/10.5194/angeo-27-4023-2009>, 2009.

1697 Li, L., Mahowald, N. M., Miller, R. L., Pérez García-Pando, C., Klose, M., Hamilton, D. S.,  
1698 Gonçalves Ageitos, M., Ginoux, P., Balkanski, Y., Green, R. O., Kalashnikova, O., Kok, J. F.,  
1699 Obiso, V., Paynter, D., and Thompson, D. R.: Quantifying the range of the dust direct radiative  
1700 effect due to source mineralogy uncertainty, *Atmos. Chem. Phys.*, 21, 3973–4005,  
1701 <https://doi.org/10.5194/acp-21-3973-2021>.

1702 [Liu, Y. and Daum, P. H.: Relationship of refractive index to mass density and self-consistency of](#)



1703 [mixing rules for multicomponent mixtures like ambient aerosols, \*J. Aerosol Sci.\*, 39, 974–986,](#)  
1704 <https://doi.org/10.1016/j.jaerosci.2008.06.006>, 2008.

1705 Loeb, N. G., Doelling, D. R., Wang, H., Su, W., Nguyen, C., Corbett, J. G., Liang, L., Mitrescu,  
1706 C., Rose, F. G., and Kato, S.: Clouds and the Earth'S Radiant Energy System (CERES) Energy  
1707 Balanced and Filled (EBAF) top-of-atmosphere (TOA) edition-4.0 data product, *J. Clim.*, 31, 895–  
1708 918, <https://doi.org/10.1175/JCLI-D-17-0208.1>, 2018.

1709 Mahowald, N.: Aerosol indirect effect on biogeochemical cycles and climate, *Science* (80-. ), 334,  
1710 794–796, <https://doi.org/10.1126/science.1207374>, 2011.

1711 [Markel, V. A.: Introduction to the Maxwell Garnett approximation: tutorial, \*J. Opt. Soc. Am. A\*,](#)  
1712 [33, 1244, https://doi.org/10.1364/josaa.33.001244](https://doi.org/10.1364/josaa.33.001244), 2016.

1713 Matthes, K., Funke, B., Andersson, M. E., Barnard, L., Beer, J., Charbonneau, P., Clilverd, M. A.,  
1714 Dudok De Wit, T., Haberreiter, M., Hendry, A., Jackman, C. H., Kretzschmar, M., Kruschke, T.,  
1715 Kunze, M., Langematz, U., Marsh, D. R., Maycock, A. C., Misios, S., Rodger, C. J., Scaife, A. A.,  
1716 Seppälä, A., Shangguan, M., Sinnhuber, M., Tourpali, K., Usoskin, I., Van De Kamp, M.,  
1717 Verronen, P. T., and Versick, S.: Solar forcing for CMIP6 (v3.2), *Geosci. Model Dev.*, 10, 2247–  
1718 2302, <https://doi.org/10.5194/gmd-10-2247-2017>, 2017.

1719 Meinshausen, M., Vogel, E., Nauels, A., Lorbacher, K., Meinshausen, N., Etheridge, D. M., Fraser,  
1720 P. J., Montzka, S. A., Rayner, P. J., Trudinger, C. M., Krummel, P. B., Beyerle, U., Canadell, J.  
1721 G., Daniel, J. S., Enting, I. G., Law, R. M., Lunder, C. R., O'Doherty, S., Prinn, R. G., Reimann,  
1722 S., Rubino, M., Velders, G. J. M., Vollmer, M. K., Wang, R. H. J., and Weiss, R.: Historical  
1723 greenhouse gas concentrations for climate modelling (CMIP6), *Geosci. Model Dev.*, 10, 2057–  
1724 2116, <https://doi.org/10.5194/gmd-10-2057-2017>, 2017.

1725 Miller, R. L. and Tegen, I.: Climate response to soil dust aerosols, *J. Clim.*, 11, 3247–3267,  
1726 [https://doi.org/10.1175/1520-0442\(1998\)011<3247:CRTSDA>2.0.CO;2](https://doi.org/10.1175/1520-0442(1998)011<3247:CRTSDA>2.0.CO;2), 1998.

1727 [Miller, R. L. and Tegen, I.: Radiative Forcing of a Tropical Direct Circulation by Soil Dust](#)  
1728 [Aerosols, \*J. Atmos. Sci.\*, 56, 2403–2433, https://doi.org/10.1175/1520-](#)  
1729 [0469\(1999\)056<2403:RFOATD>2.0.CO;2](https://doi.org/10.1175/1520-0469(1999)056<2403:RFOATD>2.0.CO;2), 1999.

1730 [Miller, R. L.](#), Perlwitz, J., and Tegen, I.: Feedback upon dust emission by dust radiative forcing  
1731 through the planetary boundary layer, *J. Geophys. Res. D Atmos.*, 109, 1–17,

1732 <https://doi.org/10.1029/2004JD004912>, 2004a.

1733 [Miller, R. L., Perlwitz, J., and Tegen, I.: Modeling Arabian dust mobilization during the Asian](#)  
1734 [summer monsoon: The effect of prescribed versus calculated SST, Geophys. Res. Lett., 31, 1–4,](#)  
1735 <https://doi.org/10.1029/2004GL020669>, 2004b.

1736 Miller, R. L., Knippertz, P., Pérez García-Pando, C., Perlwitz, J. P., and Tegen, I.: Impact of dust  
1737 radiative forcing upon climate, in: Mineral Dust: A Key Player in the Earth System, Springer  
1738 Netherlands, 327–357, [https://doi.org/10.1007/978-94-017-8978-3\\_13](https://doi.org/10.1007/978-94-017-8978-3_13), 2014.

1739 Ming, Y., Ramaswamy, V., and Persad, G.: Two opposing effects of absorbing aerosols on global-  
1740 mean precipitation, Geophys. Res. Lett., 37, <https://doi.org/10.1029/2010GL042895>, 2010.

1741 Obiso, V., Gonçalves Ageitos, M., Pérez García-Pando, C., Schuster, G. L., Bauer, S. E., Biagio,  
1742 C. Di, Formenti, P., Perlwitz, J. P., Tsigaridis, K., and Miller, R. L.: Observationally constrained  
1743 regional variations of shortwave absorption by iron oxides emphasize the cooling effect of dust,  
1744 <https://doi.org/10.5194/egusphere-2023-1166>, 2023.

1745 [Panta, A., Kandler, K., Alastuey, A., González-Flórez, C., González-Romero, A., Klose, M.,](#)  
1746 [Querol, X., Reche, C., Yus-Díez, J., and Pérez García-Pando, C.: Insights into the single-particle](#)  
1747 [composition, size, mixing state, and aspect ratio of freshly emitted mineral dust from field](#)  
1748 [measurements in the Moroccan Sahara using electron microscopy, Atmos. Chem. Phys., 23, 3861–](#)  
1749 [3885, https://doi.org/10.5194/acp-23-3861-2023](https://doi.org/10.5194/acp-23-3861-2023), 2023.

1750 [Patterson, E. M., Gillette, D. A., and Stockton, B. H.: Complex index of refraction between 300](#)  
1751 [and 700 nm for Saharan aerosols, J. Geophys. Res., 82, 3153–3160,](#)  
1752 <https://doi.org/10.1029/jc082i021p03153>, 1977.

1753 Paulot, F., Ginoux, P., Cooke, W. F., Donner, L. J., Fan, S., Lin, M. Y., Mao, J., Naik, V., and  
1754 Horowitz, L. W.: Sensitivity of nitrate aerosols to ammonia emissions and to nitrate chemistry:  
1755 Implications for present and future nitrate optical depth, Atmos. Chem. Phys., 16, 1459–1477,  
1756 <https://doi.org/10.5194/acp-16-1459-2016>, 2016.

1757 Pérez, C., Nickovic, S., Pejanovic, G., Baldasano, J. M., and Özsoy, E.: Interactive dust-radiation  
1758 modeling: A step to improve weather forecasts, J. Geophys. Res. Atmos., 111,  
1759 <https://doi.org/10.1029/2005JD006717>, 2006.

1760 [Perez Garcia-Pando, C., Miller, R. L., Perlwitz, J. P., Rodríguez, S., and Prospero, J. M.:](#)

Deleted: 2004

Deleted: Ocko, I. B., Ramaswamy, V., and Ming, Y.: Contrasting climate responses to the scattering and absorbing features of anthropogenic aerosol forcings, J. Clim., 27, 5329–5345, <https://doi.org/10.1175/JCLI-D-13-00401.1>, 2014.

1767 [Predicting the mineral composition of dust aerosols: Insights from elemental composition](#)  
1768 [measured at the Izaj̄a Observatory, Geophys. Res. Lett., 43, 10,520-10,529,](#)  
1769 <https://doi.org/10.1002/2016GL069873>, 2016.

1770 [Perlwitz, J. P., Pérez García-Pando, C., and Miller, R. L.: Predicting the mineral composition of](#)  
1771 [dust aerosols - Part 1: Representing key processes, Atmos. Chem. Phys., 15, 11593–11627,](#)  
1772 <https://doi.org/10.5194/acp-15-11593-2015>, 2015a.

1773 [Perlwitz, J. P., Pérez García-Pando, C., and Miller, R. L.: Predicting the mineral composition of](#)  
1774 [dust aerosols - Part 2: Model evaluation and identification of key processes with observations,](#)  
1775 [Atmos. Chem. Phys., 15, 11629–11652, https://doi.org/10.5194/acp-15-11629-2015](#), 2015b.

1776 Persad, G. G., Ming, Y., and Ramaswamy, V.: The role of aerosol absorption in driving clear-sky  
1777 solar dimming over East Asia, *J. Geophys. Res.*, 119, 10,410-10,424,  
1778 <https://doi.org/10.1002/2014JD021577>, 2014.

1779 Réveillet, M., Dumont, M., Gascoïn, S., Lafaysse, M., Nabat, P., Ribes, A., Nheili, R., Tuzet, F.,  
1780 Ménégóz, M., Morin, S., Picard, G., and Ginoux, P.: Black carbon and dust alter the response of  
1781 mountain snow cover under climate change, *Nat. Commun.*, 13, [https://doi.org/10.1038/s41467-](https://doi.org/10.1038/s41467-022-32501-y)  
1782 [022-32501-y](https://doi.org/10.1038/s41467-022-32501-y), 2022.

1783 Rosenfeld, D., Rudich, Y., and Lahav, R.: Desert dust suppressing precipitation: A possible  
1784 desertification feedback loop, *Proc. Natl. Acad. Sci. U. S. A.*, 98, 5975–5980,  
1785 <https://doi.org/10.1073/pnas.101122798>, 2001.

1786 Ryder, C. L., Marengo, F., Brooke, J. K., Estelles, V., Cotton, R., Formenti, P., McQuaid, J. B.,  
1787 Price, H. C., Liu, D., Ausset, P., Rosenberg, P. D., Taylor, J. W., Choullarton, T., Bower, K., Coe,  
1788 H., Gallagher, M., Crosier, J., Lloyd, G., Highwood, E. J., and Murray, B. J.: Coarse-mode mineral  
1789 dust size distributions, composition and optical properties from AER-D aircraft measurements  
1790 over the tropical eastern Atlantic, *Atmos. Chem. Phys.*, 18, 17225–17257,  
1791 <https://doi.org/10.5194/acp-18-17225-2018>, 2018.

1792 [Samset, B. H.: Aerosol absorption has an underappreciated role in historical precipitation change,](#)  
1793 [Commun. Earth Environ., 3, https://doi.org/10.1038/s43247-022-00576-6, 2022.](#)

1794 Scanza, R. A., Mahowald, N., Ghan, S., Zender, C. S., Kok, J. F., Liu, X., Zhang, Y., and Albani,  
1795 S.: Modeling dust as component minerals in the Community Atmosphere Model: Development of

1796 framework and impact on radiative forcing, *Atmos. Chem. Phys.*, 15, 537–561,  
1797 <https://doi.org/10.5194/acp-15-537-2015>, 2015.

1798 Schuster, G. L., Dubovik, O., and Arola, A.: Remote sensing of soot carbon - Part 1: Distinguishing  
1799 different absorbing aerosol species, *Atmos. Chem. Phys.*, 16, 1565–1585,  
1800 <https://doi.org/10.5194/acp-16-1565-2016>, 2016.

1801 Sinyuk, A., [Torres, O., and Dubovik, O.: Combined use of satellite and surface observations to](#)  
1802 [infer the imaginary part of refractive index of Saharan dust, \*Geophys. Res. Lett.\*, 30,](#)  
1803 <https://doi.org/10.1029/2002GL016189>, 2003.

1804 [Sinyuk, A.](#), Sinyuk, A., Holben, B. N., Eck, T. F., Eck, T. F., M. Giles, D., M. Giles, D., Slutsker,  
1805 I., Slutsker, I., Korkin, S., Korkin, S., S. Schafer, J., S. Schafer, J., Smirnov, A., Smirnov, A.,  
1806 Sorokin, M., Sorokin, M., and Lyapustin, A.: The AERONET Version 3 aerosol retrieval algorithm,  
1807 associated uncertainties and comparisons to Version 2, *Atmos. Meas. Tech.*, 13, 3375–3411,  
1808 <https://doi.org/10.5194/amt-13-3375-2020>, 2020.

1809 Skiles, S. M. K., Flanner, M., Cook, J. M., Dumont, M., and Painter, T. H.: Radiative forcing by  
1810 light-absorbing particles in snow, <https://doi.org/10.1038/s41558-018-0296-5>, 1 November 2018.

1811 Sokolik, I. N. and Toon, O. B.: Incorporation of mineralogical composition into models of the  
1812 radiative properties of mineral aerosol from UV to IR wavelengths, *J. Geophys. Res.*, 104, 9423–  
1813 9444, <https://doi.org/Doi.10.1029/1998jd200048>, 1999.

1814 Song, C. H. and Carmichael, G. R.: Gas-particle partitioning of nitric acid modulated by alkaline  
1815 aerosol, *J. Atmos. Chem.*, 40, 1–22, <https://doi.org/10.1023/A:1010657929716>, 2001.

1816 Song, Q., Zhang, Z., Yu, H., Kok, J. F., Di Biagio, C., Albani, S., Zheng, J., and Ding, J.: Size-  
1817 resolved dust direct radiative effect efficiency derived from satellite observations, *Atmos. Chem.*  
1818 *Phys.*, 22, 13115–13135, <https://doi.org/10.5194/acp-22-13115-2022>, 2022.

1819 [Stephens, G. L., Wood, N. B., and Pakula, L. A.: On the radiative effects of dust on tropical](#)  
1820 [convection, \*Geophys. Res. Lett.\*, 31, 1–4, <https://doi.org/10.1029/2004GL021342>, 2004.](#)

1821 Strong, J. D. O., Vecchi, G. A., and Ginoux, P.: The response of the tropical Atlantic and West  
1822 African climate to Saharan dust in a fully coupled GCM, *J. Clim.*, 28, 7071–7092,  
1823 <https://doi.org/10.1175/JCLI-D-14-00797.1>, 2015.

1824 Taylor, K. E., Williamson, D., and Zwiers, F.: The sea surface temperature and sea-ice  
1825 concentration boundary conditions for AMIP II simulations, Program for Climate Model  
1826 Diagnosis and Intercomparison, Lawrence Livermore ..., 2000.

1827 [Wu, C., Lin, Z., and Liu, X.: The global dust cycle and uncertainty in CMIP5 \(Coupled Model  
1828 Intercomparison Project phase 5\) models, Atmos. Chem. Phys., 20, 10401–10425,  
1829 <https://doi.org/10.5194/acp-20-10401-2020>, 2020.](#)

1830 Zender, C. S., Newman, D., and Torres, O.: Spatial heterogeneity in aeolian erodibility: Uniform,  
1831 topographic, geomorphic, and hydrologic hypotheses, J. Geophys. Res. Atmos., 108,  
1832 <https://doi.org/10.1029/2002jd003039>, 2003.

1833 Zhang, X. L., Wu, G. J., Zhang, C. L., Xu, T. L., and Zhou, Q. Q.: What is the real role of iron  
1834 oxides in the optical properties of dust aerosols?, Atmos. Chem. Phys., 15, 12159–12177,  
1835 <https://doi.org/10.5194/acp-15-12159-2015>, 2015.

1836 [Zhao, A., Ryder, C. L., and Wilcox, L. J.: How well do the CMIP6 models simulate dust aerosols?,  
1837 Atmos. Chem. Phys., 22, 2095–2119, <https://doi.org/10.5194/acp-22-2095-2022>, 2022.](#)

1838 [Zhao, M., Golaz, J. C., Held, I. M., Guo, H., Balaji, V., Benson, R., Chen, J. H., Chen, X., Donner,  
1839 L. J., Dunne, J. P., Dunne, K., Durachta, J., Fan, S. M., Freidenreich, S. M., Garner, S. T., Ginoux,  
1840 P., Harris, L. M., Horowitz, L. W., Krasting, J. P., Langenhorst, A. R., Liang, Z., Lin, P., Lin, S.  
1841 J., Malyshev, S. L., Mason, E., Milly, P. C. D., Ming, Y., Naik, V., Paulot, F., Paynter, D., Philipps,  
1842 P., Radhakrishnan, A., Ramaswamy, V., Robinson, T., Schwarzkopf, D., Seman, C. J.,  
1843 Shevliakova, E., Shen, Z., Shin, H., Silvers, L. G., Wilson, J. R., Winton, M., Wittenberg, A. T.,  
1844 Wyman, B., and Xiang, B.: The GFDL Global Atmosphere and Land Model AM4.0/LM4.0: 1.  
1845 Simulation Characteristics With Prescribed SSTs, J. Adv. Model. Earth Syst., 10, 691–734,  
1846 <https://doi.org/10.1002/2017MS001208>, 2018a.](#)

1847 [Zhao, M., Golaz, J. C., Held, I. M., Guo, H., Balaji, V., Benson, R., Chen, J. H., Chen, X., Donner,  
1848 L. J., Dunne, J. P., Dunne, K., Durachta, J., Fan, S. M., Freidenreich, S. M., Garner, S. T., Ginoux,  
1849 P., Harris, L. M., Horowitz, L. W., Krasting, J. P., Langenhorst, A. R., Liang, Z., Lin, P., Lin, S.  
1850 J., Malyshev, S. L., Mason, E., Milly, P. C. D., Ming, Y., Naik, V., Paulot, F., Paynter, D., Philipps,  
1851 P., Radhakrishnan, A., Ramaswamy, V., Robinson, T., Schwarzkopf, D., Seman, C. J.,  
1852 Shevliakova, E., Shen, Z., Shin, H., Silvers, L. G., Wilson, J. R., Winton, M., Wittenberg, A. T.,](#)

**Deleted:** Strong, J. D. O., Vecchi, G. A., and Ginoux, P.:  
The Climatological Effect of Saharan Dust on Global  
Tropical Cyclones in a Fully Coupled GCM, J. Geophys.  
Res. Atmos., 123, 5538–5559,  
<https://doi.org/10.1029/2017JD027808>, 2018.

1858 Wyman, B., and Xiang, B.: The GFDL Global Atmosphere and Land Model AM4.0/LM4.0: 2.  
1859 Model Description, Sensitivity Studies, and Tuning Strategies, *J. Adv. Model. Earth Syst.*, 10,  
1860 735–769, <https://doi.org/10.1002/2017MS001209>, 2018b.

1861 Paul Ginoux, María Gonçalves Ageitos, Qianqian Song, Ronald L Miller, Vincenzo Obiso, and  
1862 Carlos Pérez García-Pando (2023), Implementation of dust mineralogy in the GFDL AM4.0  
1863 climate model, in preparation.

1864 [IPCC 2001, Climate Change 2001: The Scientific Basis, Summary for Policy Makers and](#)  
1865 [Technical Summary of the Working Group I Report, Intergovernmental Panel on Climate Change,](#)  
1866 [edited by: Houghton, J. T., Ding, Y., Griggs, D. J., Noguer, M., van der Linden, P. J., and Xiaosu,](#)  
1867 [D., Cambridge University Press, Cambridge, UK, 2001.](#)

1868

Page 20: [1] Deleted Qianqian Song 4/11/24 7:05:00 PM

Page 27: [2] Deleted Qianqian Song 4/11/24 7:05:00 PM

Page 27: [3] Deleted Qianqian Song 4/11/24 7:05:00 PM

Page 27: [4] Deleted Qianqian Song 4/11/24 7:05:00 PM

Page 27: [5] Deleted Qianqian Song 4/11/24 7:05:00 PM

Page 27: [6] Deleted Qianqian Song 4/11/24 7:05:00 PM

Page 27: [6] Deleted Qianqian Song 4/11/24 7:05:00 PM

Page 27: [7] Deleted Qianqian Song 4/11/24 7:05:00 PM

Page 27: [7] Deleted Qianqian Song 4/11/24 7:05:00 PM

Page 27: [7] Deleted Qianqian Song 4/11/24 7:05:00 PM

Page 27: [7] Deleted Qianqian Song 4/11/24 7:05:00 PM

Page 27: [7] Deleted Qianqian Song 4/11/24 7:05:00 PM

Page 27: [7] Deleted Qianqian Song 4/11/24 7:05:00 PM

Page 27: [7] Deleted Qianqian Song 4/11/24 7:05:00 PM

Page 27: [7] Deleted Qianqian Song 4/11/24 7:05:00 PM

Page 27: [7] Deleted Qianqian Song 4/11/24 7:05:00 PM

**Page 27: [7] Deleted      Qianqian Song      4/11/24 7:05:00 PM**

▼

**Page 27: [7] Deleted      Qianqian Song      4/11/24 7:05:00 PM**

▼

**Page 31: [8] Deleted      Qianqian Song      4/11/24 7:05:00 PM**

▼

**Page 35: [9] Deleted      Qianqian Song      4/11/24 7:05:00 PM**

▼